Weierstraß-Institut
für Angewandte Analysis und Stochastik

Leibniz-Institut im Forschungsverbund Berlin e. V.

Preprint ISSN 2198-5855

Computational framework for modeling, simulation, and optimization of geothermal energy production from naturally fractured reservoirs

Ondřej Pártl[1], Ernesto Meneses Rioseco[2]

submitted: December 3, 2025

[1] Weierstrass Institute
Anton-Wilhelm-Amo-Str. 39
10117 Berlin, Germany
E-Mail: ondrej.partl@wias-berlin.de

[2] Georg-August-Universität Göttingen
Dept. Structural Geology and Geothermics
Goldschmidtstr. 3
37077 Göttingen, Germany

and

LIAG-Institute for Applied Geophysics
Dept. Static Modeling
Stilleweg 2
30655 Hannover, Germany
E-Mail: ernesto.menesesrioseco@uni-goettingen.de

No. 3239
Berlin 2025

2020 *Mathematics Subject Classification.* 65M60, 76D55, 76S05.

Key words and phrases. Discrete fracture network, porous medium, fluid flow, heat transport, production optimization, geothermal reservoir.

Edited by
Weierstraß-Institut für Angewandte Analysis und Stochastik (WIAS)
Leibniz-Institut im Forschungsverbund Berlin e. V.
Anton-Wilhelm-Amo-Straße 39
10117 Berlin
Germany

Fax: +49 30 20372-303
E-Mail: preprint@wias-berlin.de
World Wide Web: http://www.wias-berlin.de/

Computational framework for modeling, simulation, and optimization of geothermal energy production from naturally fractured reservoirs

Ondřej Pártl, Ernesto Meneses Rioseco

Abstract

We describe an open-source computational framework for the automated search for deviated multi-well layouts in hot fracture-controlled reservoirs that sustainably optimize geothermal energy production. This search is performed via 3D simulations of groundwater flow and heat transfer. We model the reservoirs as geologically consistent, randomly generated discrete fracture networks (DFNs) in which the fractures are 2D manifolds with polygonal boundaries embedded in a 3D porous medium. The wells are modeled as line sources and sinks. The flow and heat transport in the DFN-matrix system are modeled by solving the balance equations for mass and energy, while expressing the momentum balance by the Darcy law. The spatial discretization is based on the finite element method stabilized via the algebraic flux correction. For the time discretization, we use a semi-implicit approach to enhance the solver efficiency. The optimization is performed via a gradient-free global optimization algorithm. By employing the immersed boundary method and a non-matching discretization strategy, the need for computationally expensive remeshing when altering well configurations within the reservoir is effectively eliminated, thereby enhancing the robustness of the proposed framework and enabling fully automated optimization. We present the results of our optimization tests for randomly generated DFNs consisting of thousands of fractures, considering realistic values of physical parameters. To demonstrate the analytical capabilities of our open-source framework, we use it to analyze and visualize the above optimization results and the structure of the above DFNs. The developed framework was verified and validated using a set of simplified yet purpose-specific fracture configurations relevant to geothermal energy extraction in naturally fractured reservoirs.

10.20347/WIAS.PREPRINT.3239 Berlin 2025

1 Introduction

Geothermal energy is increasingly important for sustainable heat and power generation, especially in deep, naturally fractured reservoirs (NFRs) such as the Upper Jurassic aquifer in the Greater Munich Region (GMR) and the fault damage zones of the Upper Rhine Graben in Germany [16, 33, 8]. These regions, central to Europe's decarbonization efforts, face complex subsurface conditions that challenge reliable modeling and well planning [3, 57, 37, 49].

NFRs contain highly heterogeneous fracture networks that control fluid flow and heat transport but complicate predictive modeling and well placement [43, 10, 36]. There are several well-established approaches to modeling NFRs.

Equivalent porous medium (EPM) approaches, widely used in early geothermal studies, fail to capture fracture-dominated flow, and their usage proved inadequate for accurately predicting premature thermal breakthroughs [13, 14, 30].

Discrete fracture network (DFN) modeling overcomes these limitations by explicitly representing fracture geometry and connectivity, enabling more accurate predictions and optimization of well configurations [7, 26].

Embedded Discrete Fracture Modeling (EDFM) provides computational savings by embedding fractures in structured grids [41, 52] but often underrepresents dense fracture connectivity and matrix–fracture heat exchange [51, 17].

High-fidelity 3D DFN modeling remains essential for geothermal reservoirs with complex, interconnected fractures like those in some sectors of the Upper Jurassic carbonates of the GMR. However, current DFN workflows face major bottlenecks: costly remeshing for each new well configuration, limited integration of fracture network metrics (e.g., intensity, connectivity, or percolation), and reliance on proprietary software that restricts customization [21, 34]. These limitations hinder efficient optimization of well placement, a critical step to avoid short-circuiting and thermal depletion.

Several DFN-based tools exist (e.g., *COMSOL Multiphysics®*, *FEFLOW*, *FracMan*, *DuMux*, *OpenGeoSys*, or *PorePy*) but often lack dynamic optimization capabilities and robust metric-driven validation [8, 28, 29, 27]. Commercial solutions remain closed-source and computationally expensive for iterative design, while open-source frameworks rarely link geological DFN metrics to optimization or facilitate the combined, detailed visualization of 3D fracture network metrics alongside physical processes.

This work introduces an open-source, computationally efficient framework for 3D modeling, simulation, and optimization of geothermal production from NFRs. Key contributions include: (1) mesh-independent well placement using the immersed boundary and non-matching approaches, eliminating remeshing during the optimization; (2) integration of DFN metrics (e.g., connectivity, percolation, or intensity) to evaluate simulation plausibility and constrain fracture models; (3) an optimization engine for exploring well configurations directly within static DFN geometries.

The framework also offers advanced visualization for interpreting fracture–flow and thermal dynamics, uses open-source solvers for transparency, and is validated against synthetic DFNs and realistic geothermal scenarios. Its scalability directly supports geothermal projects in complex reservoirs, such as optimizing doublets in the Upper Jurassic carbonates of the GMR and fault zones of the Upper Rhine Graben [14, 58]. By reducing computational cost and integrating geologically informed metrics, this tool advances sustainable geothermal development and can be adapted to a wide range of geological settings [22].

This paper is the second part of a two-stage research effort. The first part [47] introduced the underlying numerical methods; here, we present the complete computational framework, extended validation, and application to realistic reservoir scenarios. The paper is structured as follows: Section 2 explains the methodology; Section 3 summarizes the governing models and optimization procedure; Section 4 outlines the numerical background; Sections 5–7 describe the scenarios, DFN metrics, and results; and Section 8 concludes with insights into the optimization. The interested reader can also find additional verification and validation tests in the appendix.

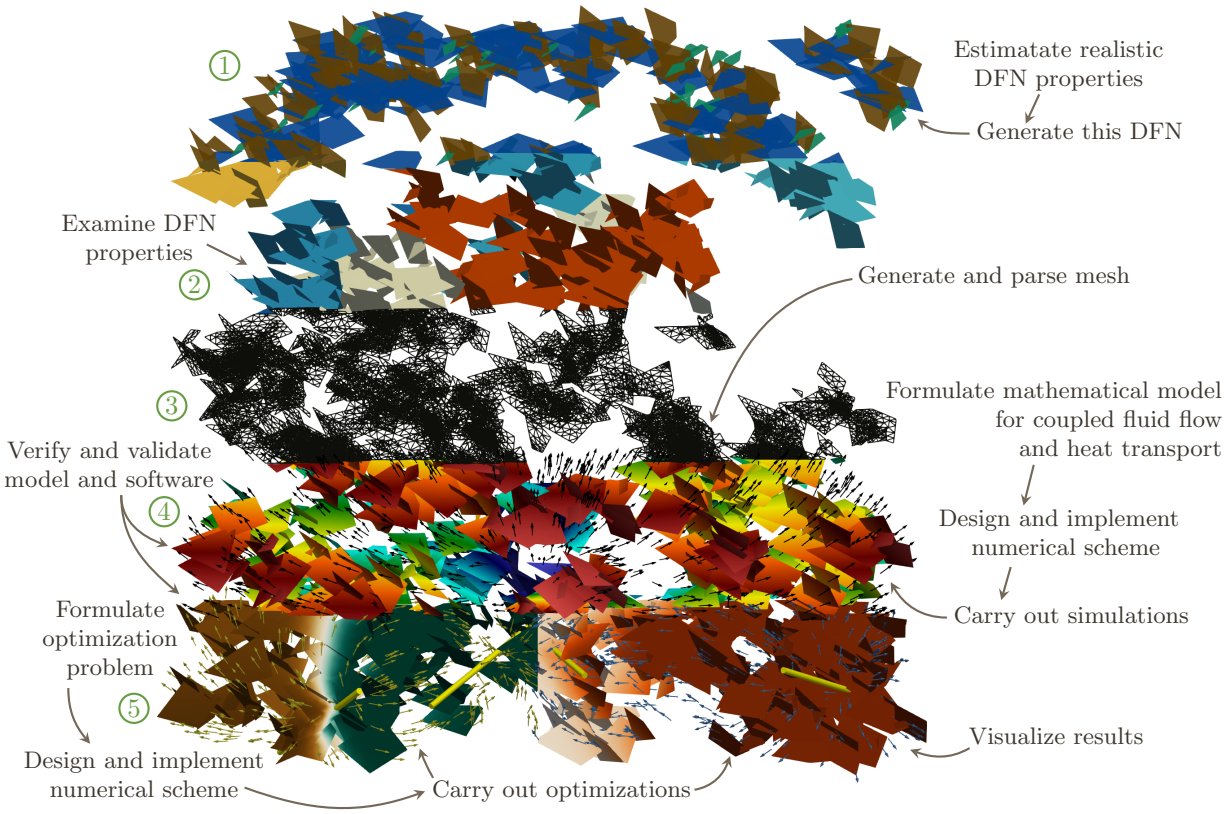

Figure 1: A DFN divided into the following sections labeled with numbers 1–5 illustrating the tasks that constitute the geothermal well placement optimization: Fracture populations (1) and clusters of interconnected fractures (2) marked with different colors. A Delaunay triangulation of the DFN (3). The fluid temperature and velocity fields resulting from a simulated operation of 4) a geothermal doublet — not displayed — and 5) two different geothermal doublets within the well-placement optimization with the wells represented by yellow cylinders.

2 Methodology

Our workflow addresses the inherently multidisciplinary nature of optimizing geothermal well placement in NFRs. It integrates geological data acquisition, DFN generation and analysis, mesh construction, coupled thermo-hydraulic simulation, optimization, visualization, and model validation (Figure 1). Below, we summarize each step and the computational tools employed.

1 **Estimation of Realistic DFN Properties.** Fracture network characteristics are derived from structural geology, hydrogeology, sedimentology, and related expertise. Generally, input data include outcrop analogues, core and log analysis, field-scale geophysical surveys, and hydraulic tests. Literature review and expert consultation ensure that physically plausible DFN parameter ranges are balanced against computational tractability.

2 **DFN Generation.** Discrete fracture networks are stochastically generated using the C++ framework *Frackit* [19], enabling specification of fracture size, orientation, and distribution.

3 **DFN Analysis and Verification.** Generated networks are analyzed with our C++ package *DFN parser*, which computes fracture statistics (e.g., size, orientation, connectivity, or percolation) and checks mesh consistency. This step ensures that the networks reflect the intended geological properties and provides reference metrics for the subsequent optimization.

4 **Mesh Generation and Parsing.** We construct triangular and tetrahedral spatial meshes using *Gmsh* and *TetGen* [18, 53]. *DFN parser* analyzes the structures of these meshes, which is essential for efficient assembly of the linear systems during the numerical solution of the balance equations.

5 **Coupled Fluid Flow and Heat Transport Simulation.**

5.1 **Mathematical Model.** We extend the 2D thermo-hydraulic model by Blank et al. [8] to 3D, capturing fracture-matrix exchange while allowing wells to be treated independently of the mesh.

5.2 **Numerical Scheme.** A finite-element formulation implemented with the *deal.II* library [1] solves mass and energy balance equations efficiently. Decoupling wells from the mesh avoids remeshing during optimization, which is crucial because each cost functional evaluation requires a full reservoir simulation over the facility's lifespan.

5.3 **Simulation Management.** We adopt a modular scenario-definition strategy, similar to the *ParMooN* framework [61], to organize parameter sets and facilitate multiple simulation runs.

6 **Well Placement Optimization.**

6.1 **Problem Formulation.** Optimization uses the cost functional proposed Blank et al. [8], minimizing thermal breakthrough risk and pressure variation.

6.2 **Optimization Algorithms.** We employ global gradient-free methods from the *NLopt* library [25], selecting algorithms compatible with our parameter constraints.

6.3 **Execution and Scenario Setup.** Well placement constraints (e.g., orientation relative to fractures in the DFN) are informed by the DFN analysis (Item 3). Our framework enables comparison of multiple algorithms by keeping scenarios free of nonlinear constraints when possible. The full optimization loop is summarized in Figure 2.

7 **Visualization.** Simulation and optimization results — including fractures, matrix properties, wells, and convergence diagnostics — are exported for 3D rendering in *VisIt* and *ParaView* [11, 4]. Output files for advanced visualization are generated with routines from *DFN parser* to ensure direct visual inspection of complex networks.

8 **Verification and Validation.** We validate the modeling and optimization workflow through systematic unit testing and scenario-based checks. Simplified synthetic DFNs enable plausibility verification of pressure and temperature fields, while progressively complex cases test scalability. Initial verification results were reported [47, 46], with additional tests provided in the appendix.

3 Mathematical model

This section briefly summarizes our mathematical model for the above system. The model follows from those by Zinsalo et al. [64] and Blank et al. [8], and it was already published by Pártl and Meneses Rioseco [47], where it is described in more detail.

We model the reservoir as a domain $\Omega \in \mathbf{R}^3$ consisting of 3D porous layers, Ω_{la}, porous fractures, Ω_{fr} (with $\Omega_{\mathrm{fr}} \subset \partial\Omega_{\mathrm{la}}$), and wells. The fractures are approximated as 2D manifolds with polygonal boundary, and the wells are modeled as thin cylinders.

Henceforth, we use the subscripts *la* and *fr* to distinguish between the objects associated with the layers and fractures, respectively. Similarly, the properties of the fractured rock are marked with the subscript *r* if necessary. The fluid properties do not have any subscripts. The components of vectors are denoted by the subscripts x, y, and z.

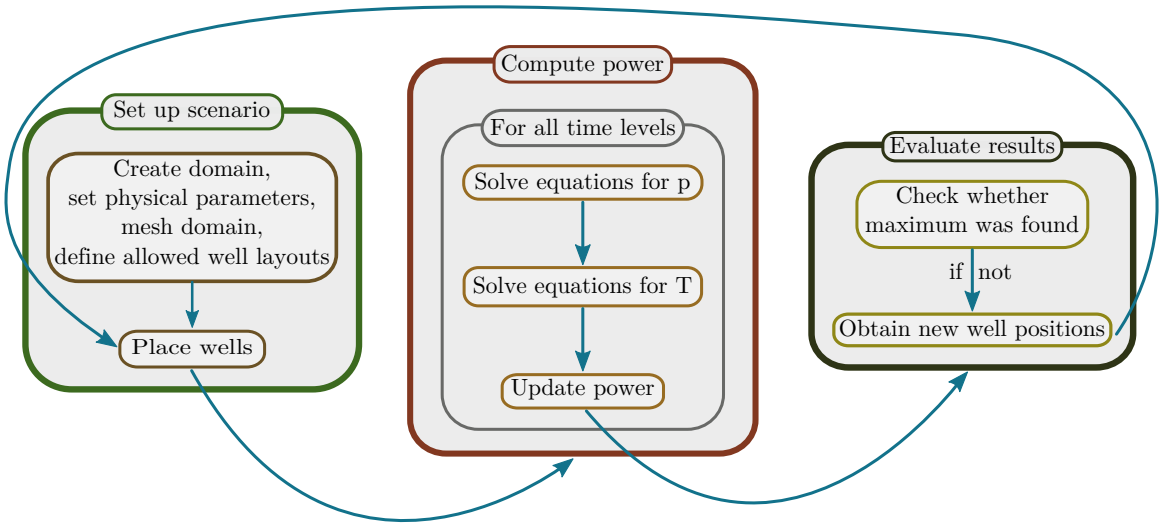

Figure 2: Schema of the optimization process. First, we set up the optimization scenario by creating the domain representing the reservoir and meshing this domain, setting the material properties, and describing what well layouts are allowed. During the optimization itself, the optimization algorithm repeats a cycle in which it selects a new well layout based on the previous results and computes the power generated by the corresponding geothermal facility. To compute the power, we simulate the operation of the geothermal facility by solving the corresponding balance equations over the operation time.

Since a well radius is at least four orders of magnitude smaller than the size of Ω, we model the wells via the immersed boundary method [48, 8]. That is, we assume that the wells are physically not present in the reservoir, and we compensate for their absence by including appropriate line mass and energy sink/source terms in the respective locations.

We consider the fractured rock non-deformable and fully saturated with a single-phase incompressible Newtonian fluid, the substances being in local thermal equilibrium. The incompressibility assumption is justified by the negligible pressure dependence of water density under typical low-enthalpy geothermal conditions.

In accordance with these assumptions, we model the fluid flow and heat transport in the reservoir by solving the corresponding balance equations for mass and energy while expressing the momentum balance by the Darcy law. All of these equations are well-established in the literature [12, 9, 55, 44, 15, 64].

3.1 Balance equations

In Ω_{la}, the equations read

$$\varepsilon_r \frac{\partial \rho}{\partial t} + \nabla \cdot (\rho \boldsymbol{v}) = S_{\mathrm{MW}}, \tag{1}$$

$$\boldsymbol{v} = -\frac{1}{\mu} \boldsymbol{k} (\nabla p - \rho \boldsymbol{g}), \tag{2}$$

$$(\rho c_p)_{\mathrm{eff}} \frac{\partial T}{\partial t} + \rho c_p \boldsymbol{v} \cdot \nabla T - \nabla \cdot \left(\lambda_{\mathrm{eff}} \nabla T \right) = S_{\mathrm{EW}}. \tag{3}$$

In (1), ε_r [−] denotes the porosity, ρ [kg · m^{-3}] is the density, t [s] represents the time, $\boldsymbol{v}$ [m · s^{-1}] stands for the fluid velocity, and S_{MW} [kg · m^{-3} · s^{-1}] is the sum of the sources/sinks of mass due to wells.

In (2), μ [Pa · s] denotes the dynamic viscosity of the fluid, and $\boldsymbol{k}$ [m^2] is the permeability tensor of the rock, which we assume to be isotropic and heterogeneous, i.e, $\boldsymbol{k} = k\boldsymbol{I}$, where the permeability coefficient k is a

scalar function, and $\boldsymbol{I}$ stands for the identity tensor. The function p [Pa] is the fluid pressure, and $\boldsymbol{g}$ [$\mathrm{m} \cdot \mathrm{s}^{-2}$] denotes the gravitational acceleration vector.

In (3), c_p [$\mathrm{J} \cdot \mathrm{kg}^{-1} \cdot \mathrm{K}^{-1}$] represents the specific heat at constant pressure of the fluid, T [K] is the common thermodynamic temperature of the fluid and the rock, c_r [$\mathrm{J} \cdot \mathrm{kg}^{-1} \cdot \mathrm{K}^{-1}$] is the specific heat of the rock, λ [$\mathrm{W} \cdot \mathrm{m}^{-1} \cdot \mathrm{K}^{-1}$] denotes the thermal conductivity coefficient, and S_{EW} [$\mathrm{J} \cdot \mathrm{m}^{-3} \cdot \mathrm{s}^{-1}$] is the source of energy due to wells.

The subscript *eff* indicates the following combination of the properties of the fluid and rock:

$$\lambda_{\mathrm{eff}} = (1-\varepsilon_r)\lambda_r + \varepsilon_r \lambda, \quad \text{and} \quad (\rho c_p)_{\mathrm{eff}} = (1-\varepsilon_r)\rho_r c_r + \varepsilon_r \rho c_p. \tag{4}$$

The terms S_{MW} and S_{EW} are defined below.

In Ω_{fr}, our equations read

$$d_{\mathrm{fr}}\varepsilon_r \frac{\partial \rho}{\partial t} + d_{\mathrm{fr}} \nabla_{\boldsymbol{t}} \cdot (\rho \boldsymbol{v}) = S_{\mathrm{MW}} + (\rho \boldsymbol{v})_{\mathrm{la}} \cdot \boldsymbol{n}^+ + (\rho \boldsymbol{v})_{\mathrm{la}} \cdot \boldsymbol{n}^-, \tag{5}$$

$$\boldsymbol{v} = -\frac{1}{\mu} \boldsymbol{k} (\nabla_{\boldsymbol{t}} p - \rho \boldsymbol{g}_{\boldsymbol{t}}), \tag{6}$$

$$d_{\mathrm{fr}}(\rho c_p)_{\mathrm{eff}} \frac{\partial T}{\partial t} + d_{\mathrm{fr}} \rho c_p \boldsymbol{v} \cdot \nabla_{\boldsymbol{t}} T - d_{\mathrm{fr}} \nabla_{\boldsymbol{t}} \cdot \left(\lambda_{\mathrm{eff}} \nabla_{\boldsymbol{t}} T \right) = S_{\mathrm{EW}} + \boldsymbol{q}_{\mathrm{la}} \cdot \boldsymbol{n}^+ + \boldsymbol{q}_{\mathrm{la}} \cdot \boldsymbol{n}^-, \tag{7}$$

where

$$\boldsymbol{q} = -\left(\lambda_{\mathrm{eff}} \nabla T \right), \tag{8}$$

and $\boldsymbol{n}^{\pm}$ stands for the unit outward normal to the fracture ($\boldsymbol{n}^+ + \boldsymbol{n}^- = 0$). The terms $\rho \boldsymbol{v} \cdot \boldsymbol{n}^{\pm}$ and $\boldsymbol{q} \cdot \boldsymbol{n}^{\pm}$ on the right-hand side of (5) and (7) are the fluxes entering/leaving Ω_{fr} through $\partial\Omega_{\mathrm{la}}$.

The symbol d_{fr} [m] denotes the (piecewise constant) fracture aperture, and the subscript $\boldsymbol{t}$ indicates the direction of the unit vector tangential to the fracture. We have $\boldsymbol{g}_{\boldsymbol{t}} = \boldsymbol{g} - \left(\boldsymbol{g} \cdot \boldsymbol{n}^+ \right) \boldsymbol{n}^+$ and, for a scalar-valued function f and a vector-valued function F,

$$\nabla_{\boldsymbol{t}} f = \nabla f - \left(\nabla f \cdot \boldsymbol{n}^+ \right) \boldsymbol{n}^+ \quad \text{and} \quad \nabla_{\boldsymbol{t}} \cdot F = \left(\boldsymbol{I} - \boldsymbol{n}^+ \otimes \boldsymbol{n}^+ \right) : \nabla F.$$

The wells are cylindrical. Each well w is characterized by its type (injection or production), position, orientation, height H_w [m], radius r_w [m], efficiency of its pump ε_w [-], and the flow rate Q_w [$\mathrm{m}^3 \cdot \mathrm{s}^{-1}$] of the fluid inside (for an injection well, $Q_w > 0$; for a production well, $Q_w < 0$). This fluid has the density ρ_w [$\mathrm{kg} \cdot \mathrm{m}^{-3}$], temperature T_w [K], and specific heat capacity at constant pressure $c_{p,w}$ [$\mathrm{J} \cdot \mathrm{kg}^{-1} \cdot \mathrm{K}^{-1}$]. The properties of each well are constant.

For any given sets of injection and production wells denoted by $\mathcal{W}_{\mathrm{inj}}$ and $\mathcal{W}_{\mathrm{pro}}$, respectively, the sink/source terms S_{MW} [$\mathrm{kg} \cdot \mathrm{m}^{-3} \cdot \mathrm{s}^{-1}$] and S_{EW} [$\mathrm{J} \cdot \mathrm{m}^{-3} \cdot \mathrm{s}^{-1}$] (in Ω_{la}) and S_{MW} [$\mathrm{kg} \cdot \mathrm{m}^{-2} \cdot \mathrm{s}^{-1}$] and S_{EW} [$\mathrm{J} \cdot \mathrm{m}^{-2} \cdot \mathrm{s}^{-1}$] (in Ω_{fr}) are approximated as

$$S_{\mathrm{MW}} = \sum_{w \in \mathcal{W}_{\mathrm{inj}} \cup \mathcal{W}_{\mathrm{pro}}} \rho_w C_w \delta_w \ \text{ and } \ S_{\mathrm{EW}} = C_{\mathrm{pen}} \sum_{w \in \mathcal{W}_{\mathrm{inj}}} C_w (\rho c_p)_w \left(T_w - T \right) \delta_w, \tag{9}$$

where δ_w [m^{-2}] stands for the Dirac delta function, and the quantities C_w [m^2/s] (in Ω_{la}) and C_w [m^3/s] (in Ω_{fr}) depend on the shape of the well w, on Q_w, and on the structure of the underlying fractured porous medium.

Note that the definition of S_{EW} originates from prescribing $T := T_w$ in the well location via a penalty method, C_{pen} [-] being a positive penalty parameter.

The information transfer between Ω_{la} and Ω_{fr} is ensured by the terms $(\rho \boldsymbol{v})_{\mathrm{la}} \cdot \boldsymbol{n}$ and $\boldsymbol{q}_{\mathrm{la}} \cdot \boldsymbol{n}$ in (5) and (7) and by an additional assumption that p and T are continuous at the interface between the layers and fractures.

On the boundaries $\partial\Omega_{\mathrm{la}}$ and $\partial\Omega_{\mathrm{fr}}$, we prescribe the flux boundary conditions

$$\rho \boldsymbol{v} \cdot \boldsymbol{n} = q_{\mathrm{M}} \quad \text{and} \quad \boldsymbol{q} \cdot \boldsymbol{n} = q_{\mathrm{E}} \tag{10}$$

and the Dirichlet boundary condition for p and T. We consider $q_{\mathrm{M}} = q_{\mathrm{E}} = 0$ on the whole $\partial\Omega_{\mathrm{fr}}$.

As for the intersections between the fractures, every common intersection of N fractures $\omega_1, \dots, \omega_N$ is assumed to be a line segment. Let $\boldsymbol{n}^s_{\partial i}$ be the unit outward normal corresponding to the side $s \in \{+,-\}$ of this intersection inside the fracture ω_i. We prescribe

$$\sum_{i\in\{1,2,\dots,N\}} \sum_{s\in\{+,-\}} d_{\mathrm{fr},i} (\rho \boldsymbol{v})_{\mathrm{fr}} \cdot \boldsymbol{n}^s_{\partial i} = 0 \qquad \text{and} \qquad \sum_{i\in\{1,2,\dots,N\}} \sum_{s\in\{+,-\}} d_{\mathrm{fr},i} \boldsymbol{q}_{\mathrm{fr}} \cdot \boldsymbol{n}^s_{\partial i} = 0. \tag{11}$$

The fluid properties ρ, μ, c_p, and λ are generally considered T-dependent, as in the simulations by Pártl and Meneses Rioseco [47, 46]. Nevertheless, for simplicity, we will consider them constant in this article.

We solve the balance equations on the time interval $[t_{\mathrm{ini}}, t_{\mathrm{fin}}]$. The primary variables are p and T, and the corresponding initial conditions are p_{ini} and T_{ini}.

3.2 Optimization

We optimize the well placement by changing only the position, orientation, and length of the wells. We consider the optimal placement to be the one that maximizes the power $\mathcal{P}$ [W] of the geothermal facility. For given sets of injection and production wells $\mathcal{W}_{\mathrm{inj}}$ and $\mathcal{W}_{\mathrm{pro}}$, we have

$$\mathcal{P}(\mathcal{W}_{\mathrm{inj}}, \mathcal{W}_{\mathrm{pro}}) = \frac{1}{t_{\mathrm{fin}} - t_{\mathrm{ini}}} \int_{t_{\mathrm{ini}}}^{t_{\mathrm{fin}}} \left(E_{\mathsf{prod}}(t, \mathcal{W}_{\mathrm{inj}}, \mathcal{W}_{\mathrm{pro}}) - E_{\mathsf{pump}}(t, \mathcal{W}_{\mathrm{inj}}, \mathcal{W}_{\mathrm{pro}}) \right) \mathrm{d}t, \tag{12}$$

where E_{prod} [J/s] is the flux of energy through the wells,

$$E_{\mathsf{prod}}(t, \mathcal{W}_{\mathrm{inj}}, \mathcal{W}_{\mathrm{pro}}) = \sum_{w\in\mathcal{W}_{\mathrm{pro}}} (\rho c_p T)|_w(t) \, |Q_w| - \sum_{w\in\mathcal{W}_{\mathrm{inj}}} \rho_w c_{p,w} T_w Q_w, \tag{13}$$

and E_{pump} [J/s] represents the energy needed for the operation of the water pumps,

$$E_{\mathsf{pump}}(t, \mathcal{W}_{\mathrm{inj}}, \mathcal{W}_{\mathrm{pro}}) = \sum_{w\in\mathcal{W}_{\mathrm{inj}}\cup\mathcal{W}_{\mathrm{pro}}} \frac{Q_w}{\varepsilon_w} \left| \Delta p|_w(t) \right| . \tag{14}$$

In (14), $\Delta p|_w$ [Pa] is the average of $p - p_{\mathrm{ini}}$ over the cylindrical well.

4 Numerical solution

This section briefly summarizes the approaches we employ to solve our balance equations and the optimization problem numerically. These approaches are the same as those by Pártl and Meneses Rioseco [47], where they are described in detail. Our choice of numerical techniques for the solution of the balance equations was motivated primarily by the requirement of short computing time because one solution over $[t_{\mathrm{ini}}, t_{\mathrm{fin}}]$ represents one evaluation of the power $\mathcal{P}$ during the optimization.

We perform the time discretization via a semi-implicit scheme, which is derived by applying the implicit Euler method modified by evaluating some terms at the old time level instead of the new one to get a linear system of equations for p and T.

For the spatial discretization, we employ the continuous finite element method with P_1 elements and solve the balance equations only for p and T, using the Darcy equations (2) and (6) as explicit formulas for the velocity.

DFN	population nr.	strike angle [°]	dip angle [°]	size [m]	ε_r [-]	k [m^2]	d_{fr} [m]
$\mathrm{DFN}^{\square}$	1	-45 ± 3	60 ± 3	70 ± 3	0.03	2.083333e-9	2.0e-4
	2	45 ± 3	-60 ± 3				
	3	0 ± 3	50 ± 3				
$\mathrm{DFN}^{\leftrightsquigarrow}$	1	-45 ± 3	60 ± 3	40 ± 3	0.035	1.302083e-10	5.0e-5
	2	45 ± 3	-60 ± 3	70 ± 3	0.05	5.208333e-10	1.0e-4
	3	0 ± 3	50 ± 3	90 ± 3	0.02	2.083333e-11	2.0e-5

Table 1: Strike and dip angles (see Figure 3), size (the largest distance between two points in the fracture), porosity ε_r, permeability coefficient k, and aperture d_{fr} of individual populations in DFNs. The notation ± 3 means the addition of a random number from $[-3, 3]$. The values were inspired by realistic DFN properties [42, 35, 50, 56]. The values of k were computed from d_{fr} via the cubic law.

The energy balance equations are stabilized using the algebraic flux correction [6, 23]. To avoid remeshing the domain when changing the positions of the wells, we decouple the wells from the spatial mesh via the non-matching approach [48, 8]. The resulting system of linear algebraic equations is solved by the BiCGSTAB with the Jacobi preconditioner.

The optimization problem is solved via the deterministic, gradient-free global optimization algorithm DIRECT from the library *NLopt* [25], where the integral in (12) is approximated using the trapezoidal rule.

The resulting numerical solver was implemented in C++ using *Deal.II* [1] and *NLopt* [25]. We carried out the simulations on the computer HPE Synergy 480 Gen10 Plus with 2 Xeon eighteen-core processors, 3000 MHz, 768 GB RAM. The systems of linear algebraic equations were solved in parallel, and the rest of the computations were performed sequentially. On average, one step of the optimization tests $\mathcal{O}_2^{\square}$, $\mathcal{O}_2^{\leftrightsquigarrow}$, and $\mathcal{O}_6^{\leftrightsquigarrow}$ described in Section 5.5 took 10.2 min, 13.3 min, and 11.9 min, respectively. Roughly 93% of each time was spent (sequentially) assembling the linear systems, which leaves room for improvement via further parallelization.

5 Definitions of scenarios and model setups

The following sections present setups of several optimization tests of our framework. Their results are discussed in Section 7.

5.1 Reservoirs

We considered 2 reservoirs ($\mathcal{R}^{\square}$ and $\mathcal{R}^{\leftrightsquigarrow}$) with $\overline{\Omega_{\mathrm{la}}^{\square}} = \overline{\Omega_{\mathrm{la}}^{\leftrightsquigarrow}} = [0, 5] \times [0, 5] \times [-4.3, -3.8]$ (in km) and DFNs ($\mathrm{DFN}^{\square}$ and $\mathrm{DFN}^{\leftrightsquigarrow}$) based on 2 versions of Ω_{fr} ($\Omega_{\mathrm{fr}}^{\leftrightsquigarrow} \neq \Omega_{\mathrm{fr}}^{\square}$) randomly generated using Frackit [19]. Each reservoir contained 6000 fractures of 3 populations (2000 fractures of each population) uniformly distributed in $\Omega_{\#} = [2, 3] \times [2, 3] \times [-4.28, -3.82]$ (in km) under the following constraints: The minimum distance between two fractures of the same populations was 1 m. For fracture intersections, the minimum intersection angle and length were $10°$ and 1 m, and the distance of the intersection from the boundaries of the fractures was at least 1 m. The properties of the fracture populations are listed in Tables 1 and 2. The networks $\mathrm{DFN}^{\square}$ and $\mathrm{DFN}^{\leftrightsquigarrow}$ are depicted in Figures 4 and 5.

We consider the fluid density in all reservoirs to be constant, making the pressure field time-independent. The invariant fluid properties are listed in Table 2.

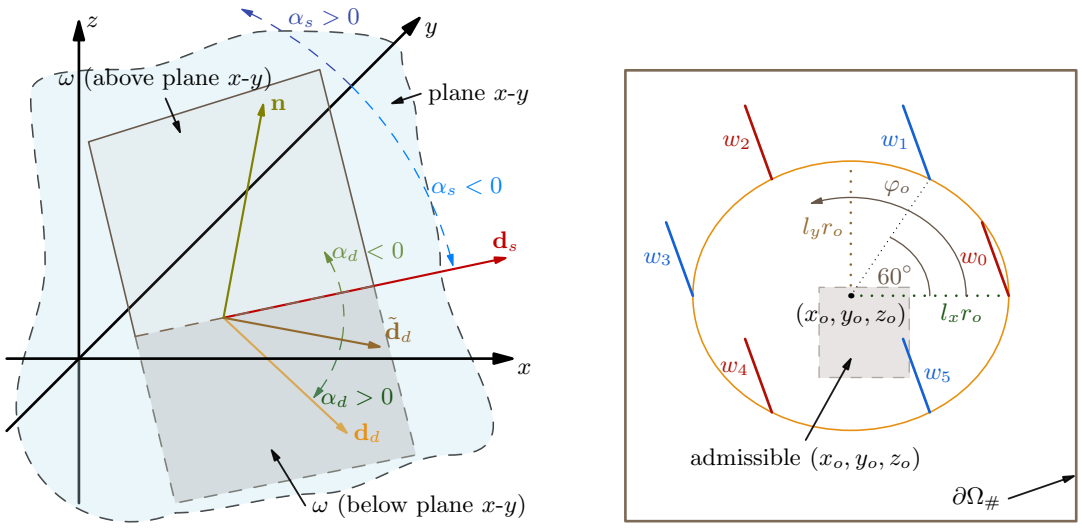

Figure 3: **Left:** Definitions of the oriented strike (α_s) and dip (α_d) angles for a given fracture ω with the normal vector $\boldsymbol{n}$ (where we assume $\boldsymbol{n}_z \geq 0$). The strike direction, $\boldsymbol{d}_s$, is the direction of the intersection of ω with the plane x-y, where we choose $\boldsymbol{d}_{s,y} \geq 0$. For given $\boldsymbol{n}$ and $\boldsymbol{d}_s$, the dip direction, $\boldsymbol{d}_d$, is determined so that $\boldsymbol{d}_d \times \boldsymbol{d}_s = \boldsymbol{n}$. The vector $\tilde{\boldsymbol{d}}_d$ is the projection of $\boldsymbol{d}_d$ onto the plane x-y. The strike angle is the angle between $\boldsymbol{d}_s$ and the y-axis, and the dip angle is the angle between $\boldsymbol{d}_d$ and $\tilde{\boldsymbol{d}}_d$. The signs of the angles are indicated in the figure. **Right:** The ellipse given by system (16) and the corresponding wells for the scenario $\mathcal{O}_6$ viewed from above. The center (x_o, y_o, z_o) can be moved inside the gray square. The injection wells are blue, and the production wells are red.

Parameters in (1)–(8)		
Parameter	Value	Unit
$\varepsilon_{r,\mathrm{la}}$	0.1	–
ρ	954.2	$\mathrm{kg \cdot m^{-3}}$
μ	$2.23 \cdot 10^{-4}$	$\mathrm{Pa \cdot s}$
$k_{\mathrm{la}}^{\square}$	$3.0 \cdot 10^{-16}$	$\mathrm{m^2}$
$k_{\mathrm{la}}^{\leftrightsquigarrow}$	$3.0 \cdot 10^{-17}$	$\mathrm{m^2}$
$\boldsymbol{g}$	$(0, 0, -9.81)$	$\mathrm{m \cdot s^{-2}}$
ρ_r	2730.0	$\mathrm{kg \cdot m^{-3}}$
c_r	2230.0	$\mathrm{J \cdot kg^{-1} \cdot K^{-1}}$
c_p	4169.7	$\mathrm{J \cdot kg^{-1} \cdot K^{-1}}$
λ_r	4.07	$\mathrm{W \cdot m^{-1} \cdot K^{-1}}$
λ	0.71	$\mathrm{W \cdot m^{-1} \cdot K^{-1}}$
Parameters in (9) and parameters of a well w		
C_{pen}	10^3	–
H_w	200.0	m
r_w	0.07	m
ρ_w	983.75	$\mathrm{kg \cdot m^{-3}}$
T_w	333.16	K
$c_{p,w}$	4169.7	$\mathrm{J \cdot kg^{-1} \cdot K^{-1}}$
$r_{\varepsilon,w}$	7.0	m
ε_w	0.6	–

Table 2: Values of invariant physical properties used in this study. Rock parameter values are derived from published data and reflect realistic DFN physical properties [56, 33, 13, 20, 39]. The fluid properties correspond to water at 130°C [32], and ρ_w is the density at the temperature T_w given by the approximation by Zinsalo et al. [64].

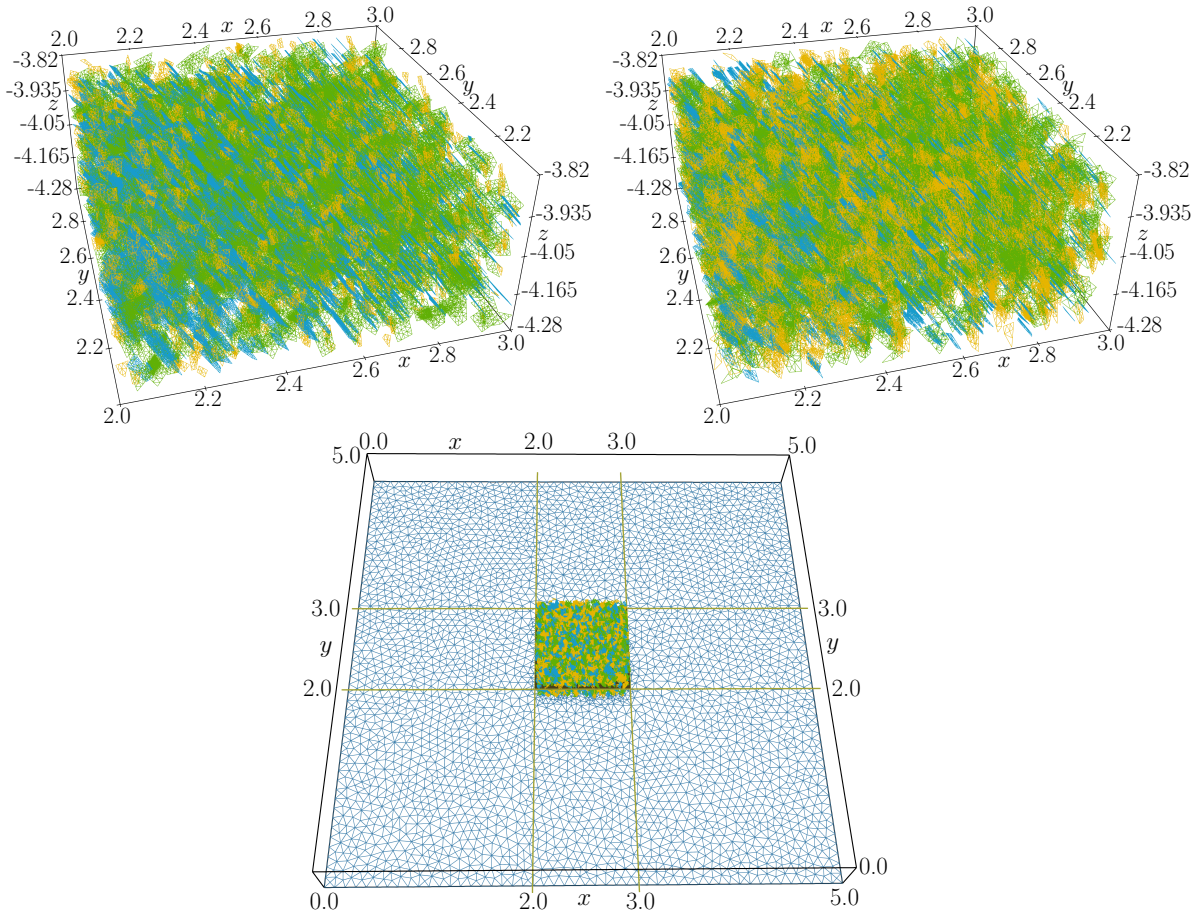

Figure 4: Triangulations covering $\mathrm{DFN}^{\square}$ (left) and $\mathrm{DFN}^{\leftrightsquigarrow}$ (right). The color indicate the fracture population numbers (orange = 1, green = 2, blue = 3). **Bottom:** The position of $\mathrm{DFN}^{\square}$ and $\mathrm{DFN}^{\leftrightsquigarrow}$ inside $\overline{\Omega_{\mathrm{la}}}$ and triangulation covering the bottom face of $\partial\Omega_{\mathrm{la}}^{\square}$. The units are km.

5.2 Initial and boundary conditions

The initial conditions are always

$$p_{\mathrm{ini}}(x,y,z) = p_{\mathrm{top}} - \rho \boldsymbol{g}_z \cdot (z - 300.0), \;\; T_{\mathrm{ini}}(x,y,z) = T_{\mathrm{top}} - T_{\mathrm{grad}} \cdot z \tag{15}$$

for $p_{\mathrm{top}} = 101325.0$ Pa (the normal pressure) and hydrostatic conditions characterized by a water table located 300 m below the surface, comparable to the hydrogeological setting of the naturally fractured Upper Jurassic carbonates in the GMR, Germany [13, 31]. Further, we set $T_{\mathrm{top}} = 283.16$ K (commonly assumed as the average annual surface temperature in temperate climates [45, 62] and $T_{\mathrm{grad}} = 0.03$ K/m (average geothermal gradient in low-enthalpy, non-magmatic geothermal play types [2, 40, 38].

On $\partial\Omega_{\mathrm{fr}}$ and on the faces of $\partial\Omega_{\mathrm{la}} \setminus \overline{\Omega_{\mathrm{fr}}}$ that are parallel to the plane x-y, we always prescribed homogeneous Neumann boundary conditions. In the remainder of $\partial\Omega_{\mathrm{la}} \setminus \overline{\Omega_{\mathrm{fr}}}$, we considered the Dirichlet boundary conditions identical to the initial conditions.

5.3 Optimization scenarios $\mathcal{O}_{2N}$

We considered the following optimization scenarios $\mathcal{O}_{2N}$ with $t_{\mathrm{ini}} = 0$ and $t_{\mathrm{fin}} = 60 \cdot 60 \cdot 24 \cdot 365 \cdot 50$ s ≈ 50 years, N injection wells and N production wells, and 5 optimization parameters describing the well positions.

The orientation of the wells was invariable: For each well, the axis of symmetry going through its bases had the direction $(\sin\omega_z \cos\omega_{xz}, \sin\omega_z \sin\omega_{xz}, -\cos\omega_z)$ for $\omega_z = \pi/3 = 60°$ and $\omega_{xz} = 11\pi/18 = 110°$, where ω_z is the angle between the well and the z-axis. The angles ω_z and ω_{xz} had been determined based on the requirement that the well should not intersect the fractures in our DFNs at an angle smaller than 30°. Determination of such directions for a given DFN is one of the features implemented in our *DFN parser*. The well flow rates Q were scenario-dependent constants defined in Section 5.5. The invariable well properties are listed in Table 2.

For each $\mathcal{O}_{2N}$, the optimization parameters were $x_o \in [2.429620,\, 2.629620]$, $y_o \in [2.318620,\, 2.518620]$, $z_o \in [-4.13,\, -3.87]$, $r_o \in [0.4,\, 1]$ (all in km), and $\varphi_o \in [0,\, 2\pi/N]$. We ordered the wells so that the i-th well, w_i, was a production well for an even i and an injection well for an odd i, where $i = 0, 1, \ldots, N-1$. For every $(x_o, y_o, z_o, r_o, \varphi_o)$, the center of the upper base of w_i was

$$\left(x_o + l_x r_o \cos\left(\varphi_o + 2i\pi/N\right),\; y_o + l_y r_o \sin\left(\varphi_o + 2i\pi/N\right),\; z_o\right),$$

where $l_x = 0.35038$ and $l_y = 0.29862$. That is, for every (x_o, y_o, z_o), the centers of the upper bases of the wells were uniformly spaced on the ellipse

$$\begin{aligned} x &= x_o + l_x r_o \cos\varphi_o, \\ y &= y_o + l_y r_o \sin\varphi_o, \\ z &= z_o. \end{aligned} \tag{16}$$

We shifted the ellipse in space and moved the wells along the ellipse, keeping the uniform spacing. The minimum distance between the wells and the lateral boundaries of $\Omega_{\#}$ was 20 m. The situation is depicted in Figure 3.

5.4 Parameters of numerical solver

We always solved the balance equations with the time step $\Delta t = (t_{\mathrm{fin}} - t_{\mathrm{ini}})/50$ s ≈ 1 year. The domains $\Omega_{\mathrm{fr}}^{\square}$ and $\Omega_{\mathrm{fr}}^{\leftrightsquigarrow}$ were covered by boundary conforming Delaunay meshes of 416128 and 462872 triangles with edge lengths in $[3.3 \cdot 10^{-3},\, 56.7]$ and $[3.7 \cdot 10^{-3},\, 27.1]$ (in m), respectively. The corresponding $\Omega_{\mathrm{la}}^{\square}$ and $\Omega_{\mathrm{la}}^{\leftrightsquigarrow}$ were covered with boundary and fracture conforming Delaunay meshes of 2174538 and 2883612 tetrahedra with

edge lengths in the intervals $[3.3 \cdot 10^{-3}, 375.0]$ and $[3.0 \cdot 10^{-4}, 371.9]$ (in m), respectively, where each triangle was a face of two tetrahedra. The wells were approximated using the artificial radius $r_\varepsilon = 7$ m (defined in the paper by Pártl and Meneses Rioseco [47]).

5.5 Optimization tests

This paper presents the following 3 optimization tests. Their results are discussed in Section 7.

$\mathcal{O}_2^{\square}$: Optimization scenario $\mathcal{O}_2$ with well flow rates $Q_2^{\square} = \pm 60\, l/s$ and reservoir $\mathcal{R}^{\square}$.

$\mathcal{O}_2^{\leftrightsquigarrow}$: Optimization scenario $\mathcal{O}_2$ with well flow rates $Q_2^{\leftrightsquigarrow} = \pm 20\, l/s$ and reservoir $\mathcal{R}^{\leftrightsquigarrow}$.

$\mathcal{O}_6^{\leftrightsquigarrow}$: Optimization scenario $\mathcal{O}_6$ with well flow rates $Q_6^{\leftrightsquigarrow} = \pm 10\, l/s$ and reservoir $\mathcal{R}^{\leftrightsquigarrow}$.

We also measured the time for the injected cold water to reach the production well, which we call the *time of thermal breakthrough occurrence*, t_{break} [year]. There is no universal definition of t_{break}. We define it as the time at which the temperature at the production well drops by more than 1 K [5].

6 Evaluation of reservoir characteristics

In naturally fractured geothermal reservoirs, the fracture network strongly governs fluid flow and heat transport, directly impacting production performance [60, 63, 59]. For the well placement optimization, an understanding of how fracture geometry shapes pressure and temperature fields is crucial.

In this study, we integrate the DFN analysis into reservoir modeling to support simulation interpretation and decision-making. This analysis is performed by a set of computational routines in our *DFN parser* that quantify and visualize key DFN metrics for a given volume enclosed by a prism. These routines mimic the analytical computations. For example, when determining a prism-fracture intersection, we find all intersections of the fracture with the faces of the prism and order these intersections to get the boundary of the desired prism-fracture intersection.

Key Fracture Network Attributes

The following DFN characteristics critically influence geothermal productivity and guide well targeting:

- **Fracture Density:** High density enhances effective permeability by connecting matrix blocks and shortening flow paths. *DFN parser* determines the number and total area of fractures intersecting selected volumes (Figure 6, Tables 3 and A.2).
- **Connectivity:** Well-connected fractures establish continuous pathways, reducing hydraulic resistance and supporting efficient circulation. *DFN parser* identifies clusters of interconnected fractures and counts intersections within (Figure 5).
- **Percolation and Flow Paths:** Beyond density, network extent and percolation determine whether fractures link injection and production wells. For each cluster of interconnected fractures, *DFN parser* estimates *cluster size* (the largest distance between two points in the cluster) and *length* (the length of the longest of the shortest paths between two points in the cluster) and determines the *cost of the best path*, $\mathcal{C}$ [1/m]:

$$\mathcal{C} = \sum_{e \in \mathcal{E}} w_e\, l_e \quad \text{for} \quad w_e = \frac{1}{k},$$

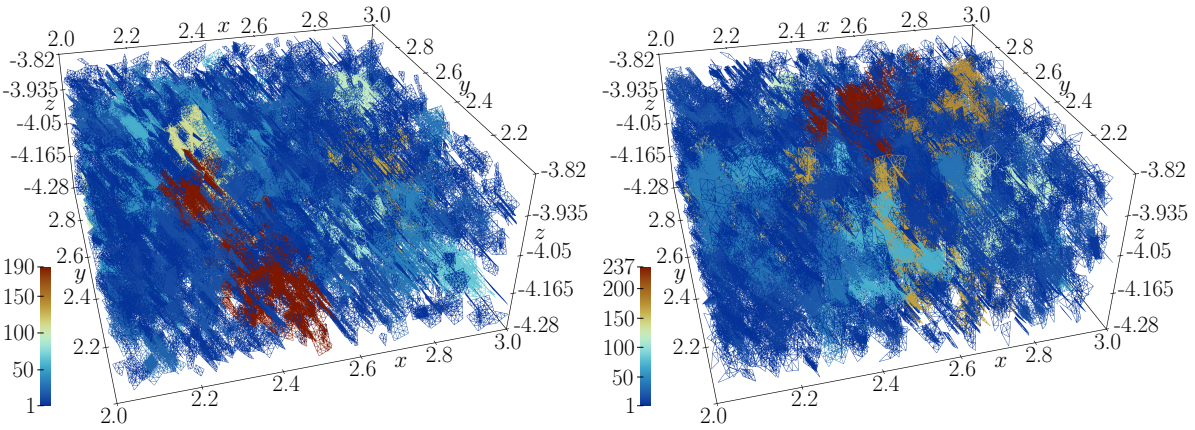

Figure 5: Triangulations covering $\mathrm{DFN}^{\square}$ (left) and $\mathrm{DFN}^{\leftrightsquigarrow}$ (right). The colors indicate the numbers of interconnected fractures forming the respective clusters.

where $\mathcal{E}$ is the set of mesh edges forming the path, l_e and w_e are the length and weight of edge e, and k denotes the average permeability of the adjacent cells (considering only 2D cells if e lies on a fracture). Lower C values indicate more favorable connections.

The computations of C and the cluster length are based on Dijkstra's algorithm applied to the spatial mesh covering $\overline{\Omega_{\mathrm{la}}}$ (Figures 9 and A.1, Table A.1). Therefore, both characteristics are estimates that improve when refining the mesh.

- **Aperture, Porosity, and Permeability:** Larger aperture and higher porosity/permeability increase flow capacity and reduce injection–production pressure differences. *DFN parser* computes averages of these properties.

- **Fracture Geometry and Orientation:** Fracture size and alignment with the pressure gradient control connectivity and thermal recovery. *DFN parser* calculates fracture size (the largest distance between two points inside) and suggests a suitable orientation of the wells based on the orientation of the fractures. These features were used when checking whether $\Omega_{\mathrm{fr}}^{\square}$ and $\Omega_{\mathrm{fr}}^{\leftrightsquigarrow}$ were generated correctly and when determining ω_z and ω_{xz} in Section 5.3.

- **Fracture–Well Intersections:** The number of fractures intersecting a well directly measures drainage efficiency and injectivity/productivity. *DFN parser* detects and visualizes these intersections (Figures 10 and 14).

By evaluating these metrics, *DFN parser* enables robust well placement strategies in highly heterogeneous fractured reservoirs. Integrating connectivity, percolation pathways, and local flow properties with simulated pressure and temperature fields informs optimization, mitigates thermal short-circuiting, and sustains long-term geothermal production.

7 Simulation results

This section presents the results of the optimization tests described in Section 5.5. To assess the plausibility of the outcomes, we visualize and compare key DFN characteristics for selected configurations evaluated during the optimization process. Unless otherwise specified, injection and production wells are shown in blue and red, respectively, in all figures.

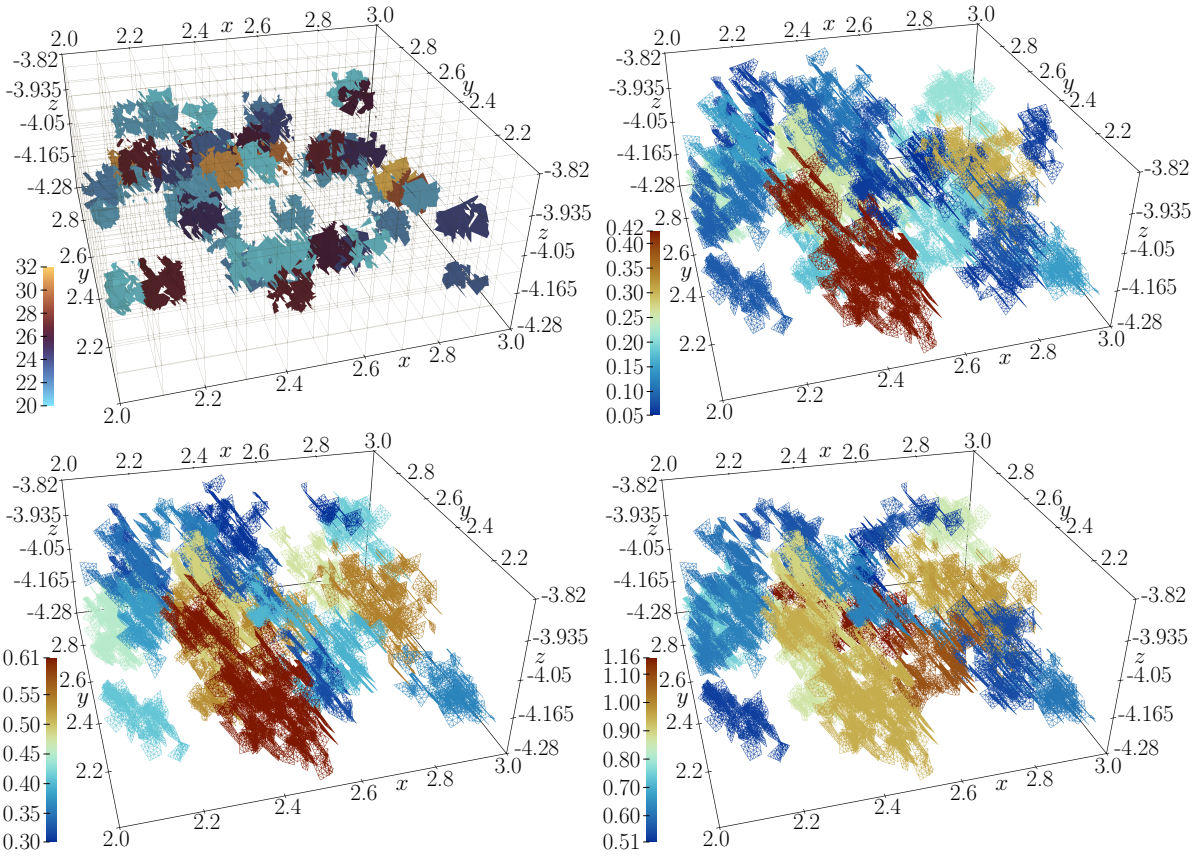

Figure 6: **Top left:** Uniform partitioning of $\overline{\Omega_\#}$ into boxes together with fractures in those boxes that contain at least 20 fracture intersections. The numbers of intersections in the boxes are expressed by colors. **Top right:** Triangulation covering $\mathrm{DFN}^{\leftrightsquigarrow}$. The colors indicate the areas [km^2] of clusters of interconnected fractures. Only clusters with an area of at least 0.05 km^2 are displayed. **Bottom left:** Triangulation covering $\mathrm{DFN}^{\leftrightsquigarrow}$. The colors indicate the diameters [km] of clusters of interconnected fractures. Only clusters with a diameter of at least 0.3 km are displayed. **Bottom right:** Triangulation covering $\mathrm{DFN}^{\leftrightsquigarrow}$. The colors indicate the lengths [km] of clusters of interconnected fractures. Only clusters with a length of at least 0.5 km are displayed. The units of the coordinate axes are km.

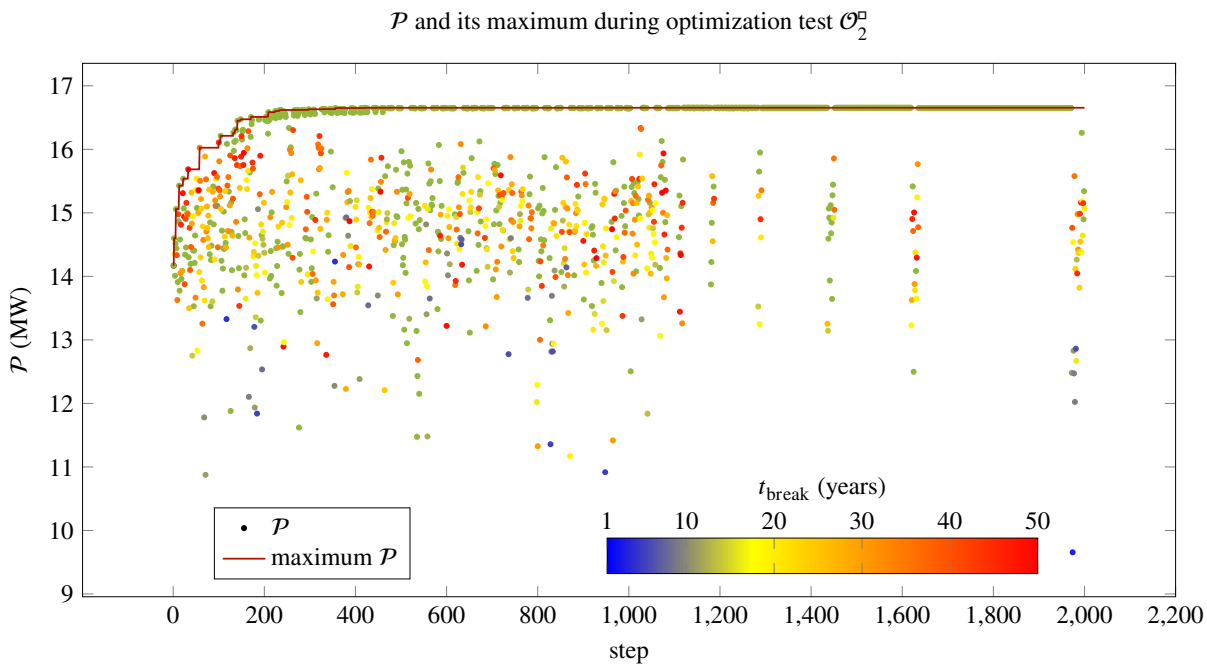

Figure 7: Power $\mathcal{P}$ and its maximum during the optimization test $\mathcal{O}_2^\square$. The colors indicate t_{break}, with the olive color corresponding to no thermal breakthrough.

7.1 Test $\mathcal{O}_2^\square$

The optimization progress is depicted in Figure 7. It shows that the algorithm spent a considerable amount of its runtime moving the wells in the immediate vicinity of the optimum instead of searching new parts of the reservoir, which we consider undesirable. This indicates there is room for improvement in the optimization algorithm. As expected, the best well placements are those for which the thermal breakthrough did not occur.

Figure 8 shows T and $p - p_{\text{ini}}$ in the fractures for the optimum well placement defined by $x_o = 2.5275$, $y_o = 2.5067$, $z_o = -4.0839$, $r_o = 0.5184$, and $\varphi_o = 3.1156$, where the optimum power was $\mathcal{P} = 16.654$ MW. The above values of z_o and r_o lie near the lower bounds of the parameter ranges. This was expected because lower z_0 corresponds to higher production temperature, and the proximity of the wells facilitates the water injection, resulting in smaller $\left|\Delta p|_w(t)\right|$ in (14). However, too small values of r_o lead to a premature thermal breakthrough.

A detailed view of the fractures intersecting the wells (not presented here) reveals that these fractures intersect the injection well mainly in its farther part, which is the reason why the injected cold water spread farther around this area. However, the cold water still remains far away from the production well. Additionally, the fracture clusters intersecting the production well are several times larger than those intersecting the injection well, resulting in a much greater area of a large difference in $p - p_{\text{ini}}$ (cf. the red and deep blue parts of the right figure in Figure 8).

To demonstrate the usage of our tools for the evaluation of the reservoir characteristics, we will describe two well layouts that are comparable in terms of z_o, the distance between the wells, the numbers of well-fracture intersections, etc. in more detail. We selected the layouts corresponding to the optimization steps 672 (where $x_o = 2.5296$, $y_o = 2.3742$, $z_o = -4.0867$, $r_o = 0.9$, $\varphi_o = 1.7453$, and $\mathcal{P} = 16.124$ MW) and 45 (where $x_o = 2.4630$, $y_o = 2.3520$, $z_o = -4.0867$, $r_o = 0.7$, $\varphi_o = 3.1416$, and $\mathcal{P} = 13.529$ MW). More quantities describing these layouts are listed in Table 3 and Figure 10.

In both layouts, the wells were placed at the same depth and intersected the same number of fractures. Although in the latter layout, the wells were placed closer to each other, the vicinity of the wells had less favorable structure,

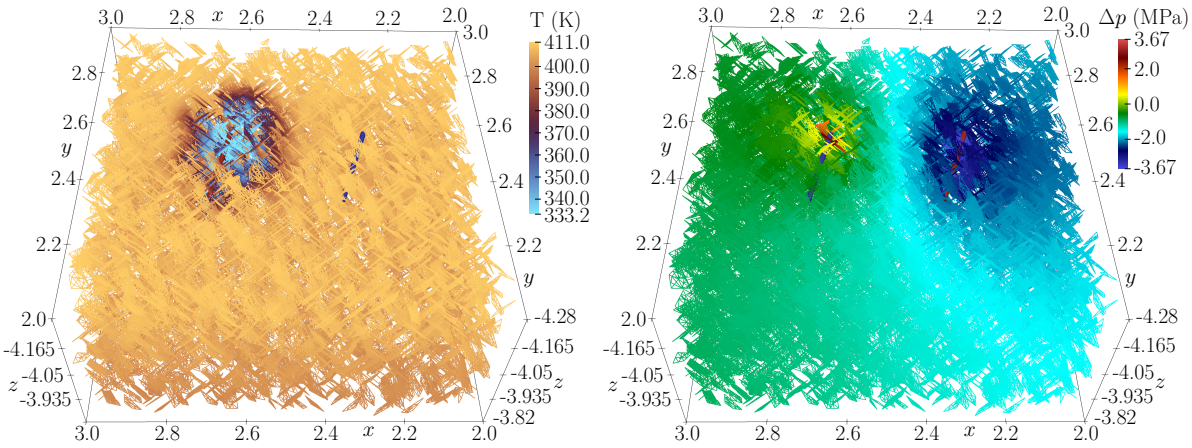

Figure 8: T and $\Delta p = p - p_{\text{ini}}$ in fractures for the optimal arrangement of the wells in test $\mathcal{O}_2^{\square}$. The color scale for Δp is bounded from below to enhance the readability. The real minimum of Δp is -8.18 MPa. The reservoir is displayed upside down to make the wells visible. The distance unit is km.

step nr.	dist.	$N_{\times}^{\text{inj}}$	$N_{\times}^{\text{pro}}$	Δp	$\rho_{\times}$	$\rho_{\lvert\#\rvert}$	C	$C_{\#}$	$\overline{C_{\text{corr}}}$
$\mathcal{O}_2^{\square}$: 672	540.56	7	7	10.28	$3.40 \cdot 10^{-5}$	0.0322	$29.9661 \cdot 10^{18}$	$29.9660 \cdot 10^{18}$	$106.57 \cdot 10^{18}$
$\mathcal{O}_2^{\square}$: 45	490.53	7	7	37.93	$2.88 \cdot 10^{-5}$	0.0311	$32.4423 \cdot 10^{18}$	$32.4421 \cdot 10^{18}$	$134.66 \cdot 10^{18}$
$\mathcal{O}_2^{\leftrightsquigarrow}$: 1331	312.37	11	11	117.98	$1.50 \cdot 10^{-5}$	0.0306	$49.2307 \cdot 10^{15}$	$91.6220 \cdot 10^{15}$	$0.58 \cdot 10^{18}$
$\mathcal{O}_2^{\leftrightsquigarrow}$: 1557	347.82	10	9	73.88	$1.54 \cdot 10^{-5}$	0.0331	$0.01 \cdot 10^{15}$	0.0	$1.19 \cdot 10^{18}$

Table 3: Quantities describing the selected layouts. They are (in this order) the step number, distance between the wells [m], number of fractures intersecting the injection and production wells denoted by $N_{\times}^{\text{inj}}$ [-] and $N_{\times}^{\text{pro}}$ [-], $\Delta p = \sum_{w \in \mathcal{W}_{\text{inj}} \cup \mathcal{W}_{\text{pro}}} \left| \Delta p|_w(t) \right|$ [MPa], density of fracture intersections in the corridor represented by $\rho_{\times}$ [1/m^3], area of fractures in the corridor per unit volume $\rho_{\lvert\#\rvert}$ [1/m], cost of the best path between the wells and between the clusters of fractures intersected by the wells denoted by C [1/m] and $C_{\#}$ [1/m], and average of the costs of all best paths between the wells starting from a selected mesh node in a well and leading within the corridor, which is labeled $\overline{C_{\text{corr}}}$ [1/m].

resulting in larger pressure difference in (14). We assessed this structure by computing various characteristics of the part of the reservoir enclosed by a corridor between the wells, see Table 3. This corridor, see Figure 9, is the smallest 4-sided prism enclosing both wells that extends by $r_{\varepsilon} + 50$ m from above and from below the plane defined by the centers of the bases of the wells.

For the former layout, all characteristics in Table 3 are better. The reason for the large difference in C_{corr} is probably the large difference in $\rho_{\times}$ and the alignment of the fractures: The blue fracture population in Figure 9 is approximately aligned in the direction from one well to the other well.

Additionally, Figure 10 shows that the total area of the clusters intersected by the wells in the first layout is significantly larger, which also decreases the above pressure difference.

7.2 Test $\mathcal{O}_2^{\leftrightsquigarrow}$

The comparison between the optimization progresses shown in Figures 7 and 11 underlines the complexity of the reservoir $\mathcal{R}^{\leftrightsquigarrow}$ and indicates that it is significantly more difficult to find suitable well layouts in $\mathcal{R}^{\leftrightsquigarrow}$ than in $\mathcal{R}^{\square}$. The reason for the lower local maxima of $\mathcal{P}$ and the lower number of well layouts where the thermal breakthrough occurred is the lower well flow rate and lower permeability, and aperture.

Figure 12 shows T and $p - p_{\text{ini}}$ for the optimum well placement defined by $x_o = 2.5948$, $y_o = 2.4632$, $z_o = -4.1144$, $r_o = 0.6418$, and $\varphi_o = 5.2360$. The corresponding optimum power was $\mathcal{P} = 5.574$ MW, and

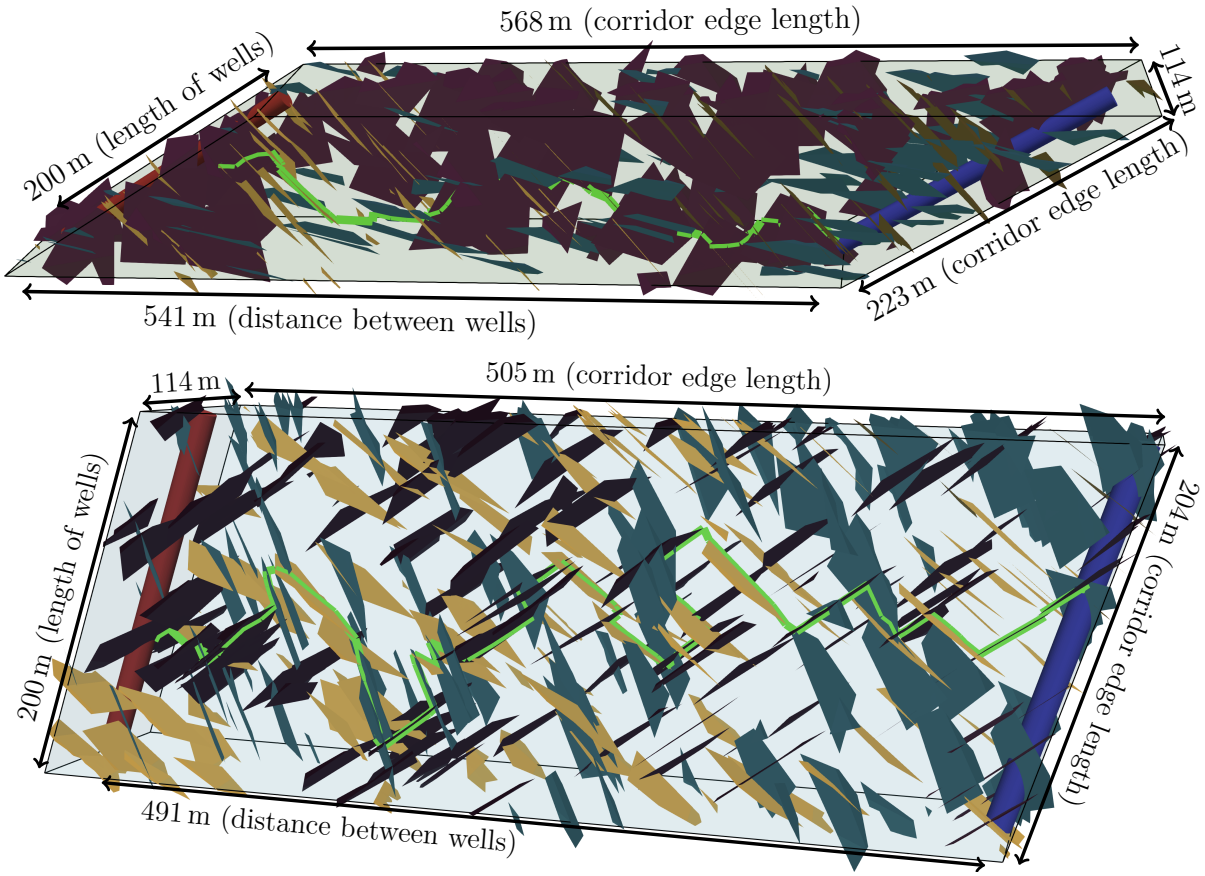

Figure 9: Corridors corresponding to the steps 672 (top) and 45 (bottom) in Figure 10. The blue fracture population in the top picture is approximately aligned in the direction from one well to the other well. The green polygonal chains represent the best paths between the wells.

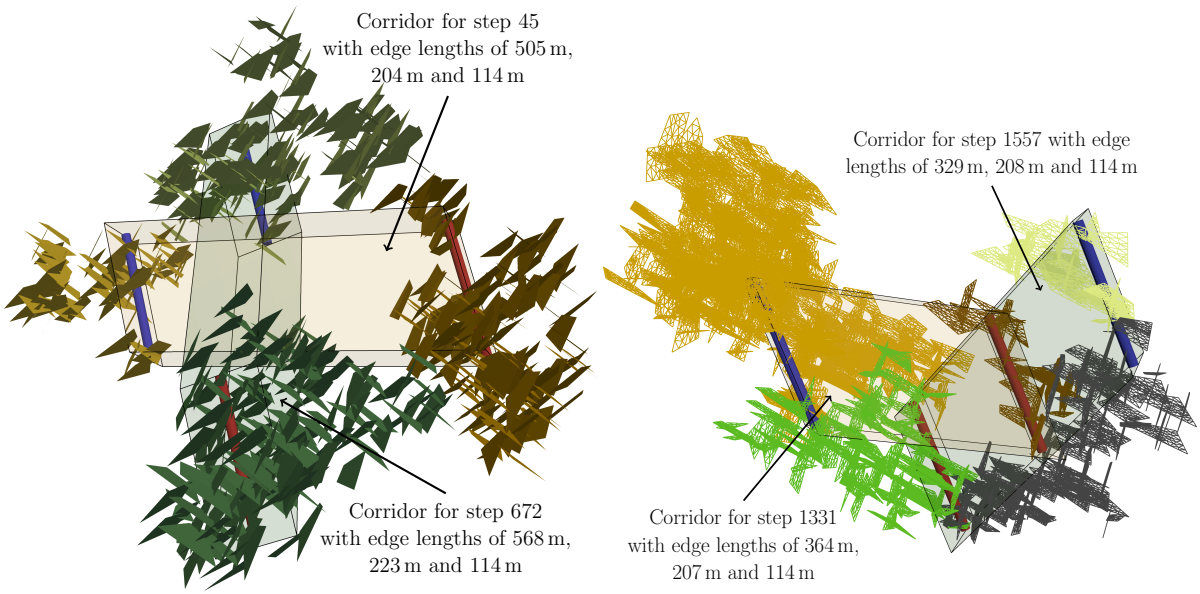

Figure 10: The clusters of fractures intersected by wells in the steps 672 (green) and 45 (ocher) in test $\mathcal{O}_2^{\square}$ (left) and in the steps 1331 (ocher) and 1557 (green and gray) in test $\mathcal{O}_2^{\leftrightsquigarrow}$ (right). The figures show the exact arrangements of the fractures and wells. In the right picture, the gray cluster is intersected by both wells in step 1557. The total areas and lengths of the clusters intersected by wells are $0.50\,\mathrm{km}^2$ and $2.57\,\mathrm{km}$ (step 45), $0.70\,\mathrm{km}^2$ and $3.29\,\mathrm{km}$ (step 672), $1.01\,\mathrm{km}^2$ and $4.21\,\mathrm{km}$ (step 1331), and $0.76\,\mathrm{km}^2$ and $4.02\,\mathrm{km}$ (step 1557).

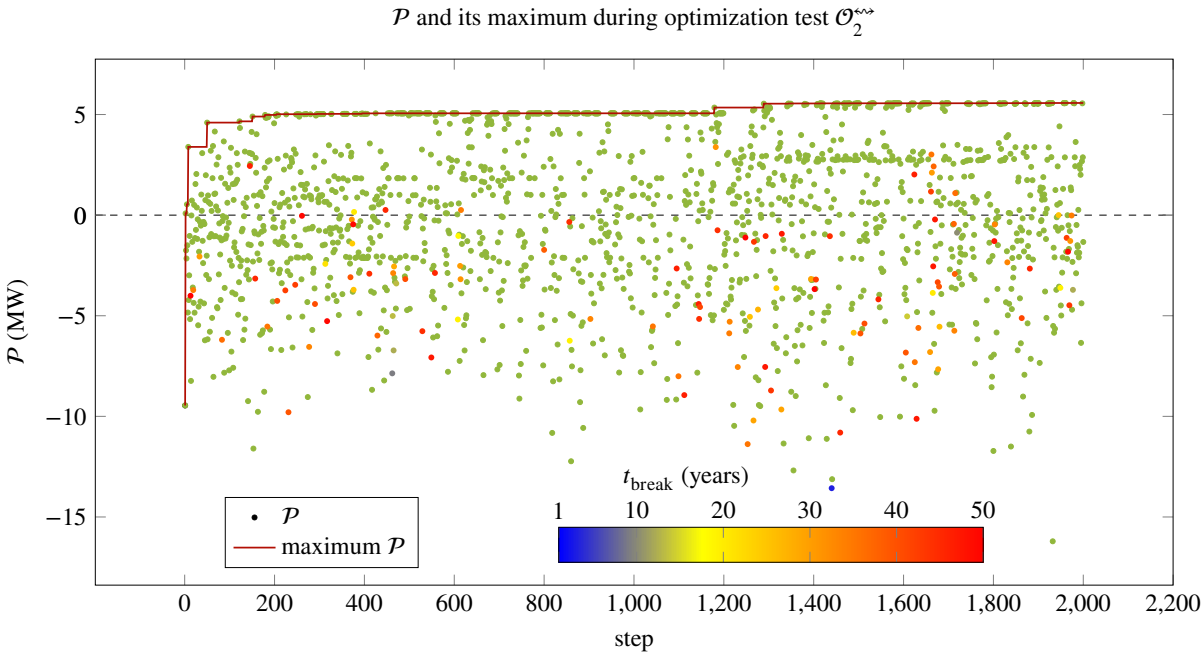

Figure 11: Power $\mathcal{P}$ during the optimization test $\mathcal{O}_2^{\leftrightsquigarrow}$. The colors indicate t_{break}, with the olive color corresponding to no thermal breakthrough.

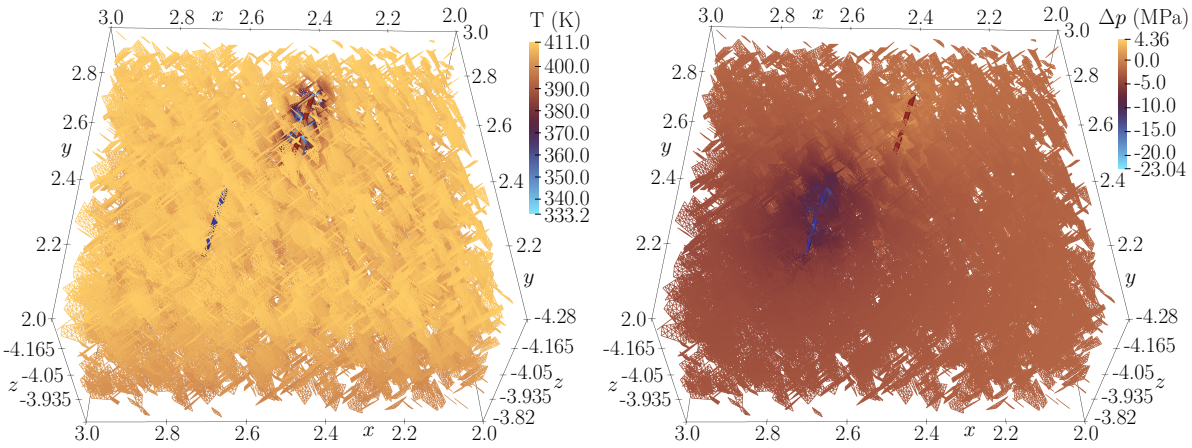

Figure 12: T and $\Delta p = p - p_{\text{ini}}$ in fractures for the optimal arrangement of the wells in test $\mathcal{O}_2^{\leftrightsquigarrow}$. The reservoir is displayed upside down to make the wells visible. The distance unit is km.

the clusters of fractures intersected by the wells (not displayed here) were only 3.5 m away from each other. Compared to Figure 8, the extrema of $p - p_{\text{ini}}$ in Figure 12 are larger due to the lower permeability and aperture. Similarly, the cold water penetrated smaller area than in Figure 8 because of the lower well flow rate.

As in Section 7.1, we will compare the well layouts in two selected optimization steps: step 1331 (where $x_o = 2.4630$, $y_o = 2.3520$, $z_o = -4.0867$, $r_o = 0.5$, $\varphi_o = 1.0472$, and $\mathcal{P} = 1.959$ MW) and 1557 (where $x_o = 2.5518$, $y_o = 2.4853$, $z_o = -4.0867$, $r_o = 0.5$, $\varphi_o = 2.909$, and $\mathcal{P} = 3.414$ MW). More quantities characterizing these layouts are listed in Table 3 and Figure 10, where the corridors are defined in the same way as in Section 7.1.

Comparing both layouts, we can see that in the former one, the wells were positioned closer to each other, and they intersected more fractures, and these fractures belonged to clusters of larger total area and length. Additionally, all wells were placed at the same depth. The former layout, nevertheless, yielded higher power because there was a cluster intersected by both wells, which resulted in smaller $\left|\Delta p|_w(t)\right|$ in (14), see Figure 10. However, a significant part of this cluster lay outside of the corridor between the wells, resulting in higher $\overline{C_{\text{corr}}}$.

7.3 Test $\mathcal{O}_6^{\leftrightsquigarrow}$

The resulting power $\mathcal{P}$ in the optimization progress depicted in Figure 13 is generally much higher than in Figure 11. The reasons are that the volume of water injected into the system is distributed between several wells, decreasing $\left|\Delta p|_w(t)\right|$ in (14), and the wells are placed closer to each other, which generally decreases $\left|\Delta p|_w(t)\right|$ as well and increases the chance of more wells intersecting the same cluster of fractures. However, the latter also resulted in a significantly larger number of steps where the thermal breakthrough occurred.

Figure 14 shows T and the clusters of fractures intersected by the wells for the optimum well layout defined by $x_o = 2.6204$, $y_o = 2.4853$, $z_o = -4.0867$, $r_o = 0.6987$, and $\varphi_o = 1.0501$, where the optimum power was $\mathcal{P} = 8.207$ MW. We can see that (as in Figure 12) the cold water also penetrated only small areas around the injection wells due to the low flow rates. The existence of 3 clusters intersecting 2 wells makes this layout particularly favorable.

8 Discussion and conclusions

We introduced two tools intended for optimization of geothermal energy production from naturally fractured reservoirs, and we presented the results obtained by applying our open-source software based on these tools

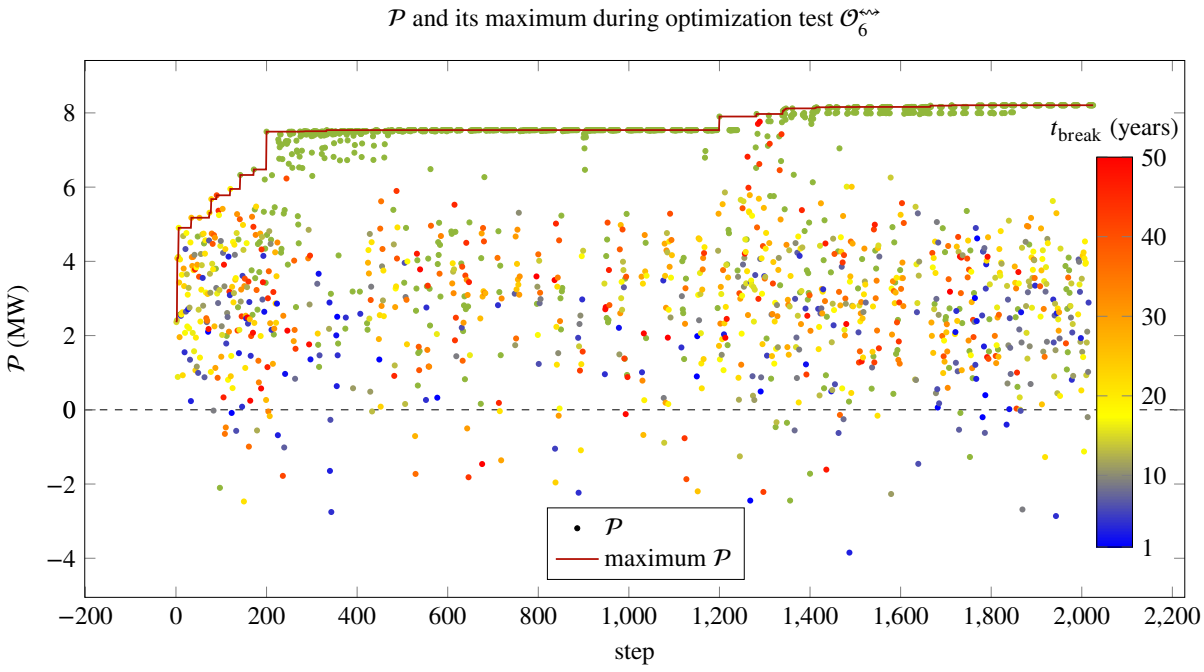

Figure 13: Power $\mathcal{P}$ during the optimization test $\mathcal{O}_6^{\leftrightsquigarrow}$. The colors indicate t_{break}, with the olive color corresponding to no thermal breakthrough.

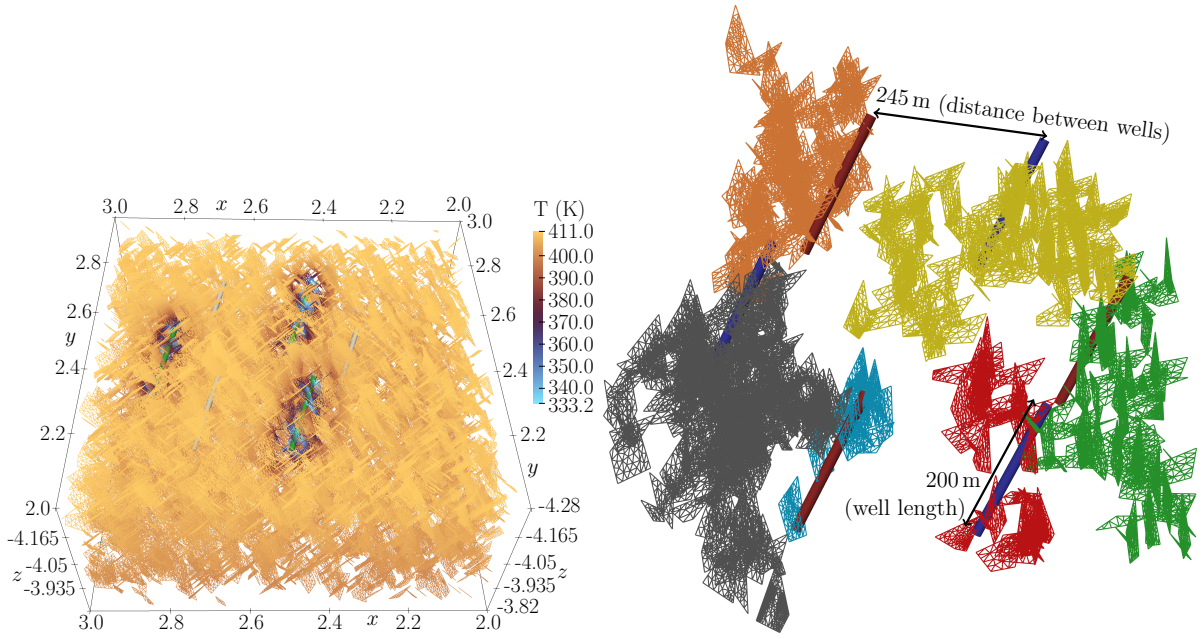

Figure 14: Optimization test $\mathcal{O}_6^{\leftrightsquigarrow}$. Temperature T and clusters intersected by wells in the optimal configuration. The injection wells are white and blue, and the production wells are green and red. In the left picture, the reservoir is displayed upside down to make the wells visible, and the distance unit is km. In the right picture, the orange, olive, and green clusters intersect two wells. The gray, blue, and red clusters intersect only one well.

to structurally complex reservoirs targeted by deviated geothermal doublets or multi-well layouts.

The first tool was a mathematical model and corresponding numerical scheme for a) 3D numerical simulation of groundwater flow and heat transport in hot fracture-controlled reservoirs and b) fully automated optimization of the placements of the injection and production wells.

The second tool was the package *DFN parser* for a) the analysis of DFNs and b) the postprocessing and visualization of DFNs and triangulations covering fracture-controlled reservoirs. For the analysis, we also proposed several metrics for the DFN characterization and implemented tools that measure them.

We showed the capability of the whole framework to find favorable well placements in complex reservoirs containing thousands of fractures of various fracture populations. But our frameworks can also be easily applied to other reservoir types, such as those dominated by dual porosity and/or dual permeability characteristic behaviors, or to heterogeneous porous media.

Our optimization framework has some limitations that open up possibilities for improvements, particularly the following:

- Fractures under in-situ subsurface conditions may deform, especially in deep DFNs under operational conditions. However, a straightforward model for poroelasticity effects can be easily included in our framework [54, 24].
- We arranged the wells in rather fixed geometrical patterns (e.g., 2 wells lying in one plane, 6 wells lying on an ellipse, etc.) to keep the dimension of the space of optimization parameters (*SOP*) and the complexity of the constraints on these parameters low, possibly ruling out many well layouts that are better than those that can be described in the same way as in Section 5. We consider this kind of simplification inevitable, at least in the case of several wells.
- Due to the runtimes listed in Section 4, our optimizations are limited to mere thousands of steps, possibly leaving many parts of the SOP unexplored. Moreover, Figure 7 shows that the optimization algorithm may start to concentrate on a very small part of the SOP, leading to the same effect.

  The former can be mitigated to some extent by parallelizing the assembly of the linear systems during the numerical solution of the balance equations. The latter may be remedied by employing other optimization algorithms.

Ultimately, verification and validation were performed using simplified yet fit-for-purpose fracture configurations to demonstrate that the computational framework reliably performs the intended modeling, simulation, and optimization tasks for geothermal energy production in naturally fractured reservoirs. The proposed open-source computational framework advances sustainable geothermal development by enabling scalable, efficient optimization of well placement in complex fractured reservoirs, removing meshing bottlenecks, and providing a robust tool adaptable to diverse geological settings worldwide.

Computer code availability

The optimizations presented in this paper were carried out employing the C++ package *Reservoir simulator* developed by one of the authors, Ondřej Pártl. This package, its description, and the input data used to produce the presented results are available in the repository https://lab.wias-berlin.de/partl/reservoir-simulator. For citation purposes, refer to the Zenodo entry https://doi.org/10.5281/zenodo.17433719.

The supporting C++ package *DFN parser* for analysis, postprocessing, and visualization of DFNs is also developed by Ondřej Pártl. This package, along with its description, examples of input data, and generated files, is available in the repository https://lab.wias-berlin.de/partl/dfn-parser. For citation purposes, refer to the Zenodo entry https://doi.org/10.5281/zenodo.17434104.

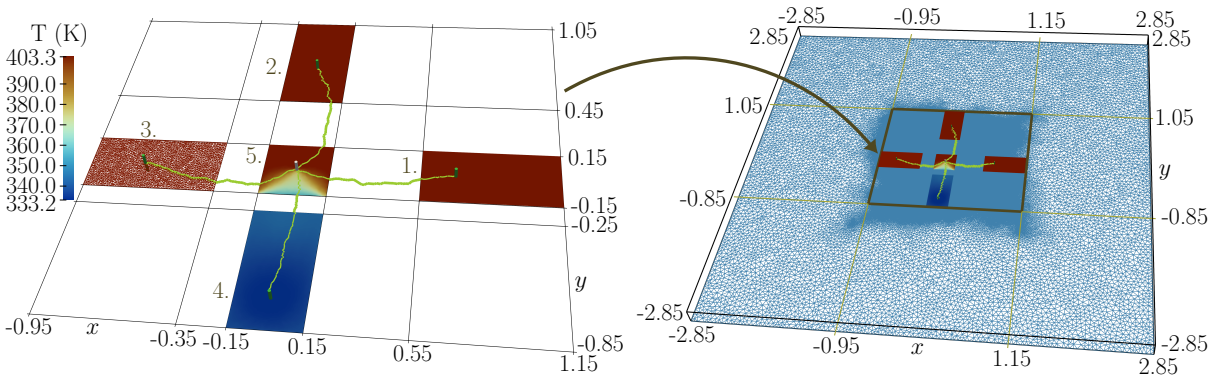

Figure A.1: **Left:** DFN consisting of 5 fractures (labeled 1.–5.), wells in four different configurations (indicated by numbers 1.–4. that coincide with the fracture labels), and the corresponding best paths between the wells. The colors of the fractures indicate the temperature T in configuration 4. The triangulation covering 3. fracture is part of the one used for the numerical solution. The fractures lie in the xy-plane, and their z-coordinates are, respectively, -3.999, -4.001, -3.9995, -4.0005, and -4.0 (in km). **Right:** Position of DFN inside $\overline{\Omega_{\mathrm{la}}}$ indicated by the black prism. The blue lines stand for the triangulation of the bottom face of $\overline{\Omega_{\mathrm{la}}}$. All spatial coordinates are in km.

Acknowledgements

This work emerged from a scientific collaboration within the Leibniz Research Network *Mathematical Modeling and Simulation* (MMS). We gratefully acknowledge the support of the Leibniz Association, Germany. This study was partly conducted within the joint research projects *WärmeGut* (Grant No. 03EE4046B) and *DEKAPALATIN-BERTHA* (Grant No. 03EXP4005B), funded by the Federal Ministry for Economic Affairs and Energy, Germany.

A Verification and validation tests

This appendix presents 2 verification and validation tests (*Paths* and *Shelves*) based on DFNs of a very simplified structure.

A.1 Paths

The purpose of this test is to check that our framework satisfies the natural requirement that the energy E_{pump} given by (14) decreases if the distance between the clusters of interconnected fractures crossed by the wells shortens. Generally, we require E_{pump} to decrease if the area between the wells is more fractured.

A.1.1 Reservoir setup

We considered $\overline{\Omega_{\mathrm{la}}} = [-2.85,\, 2.85]\times[-2.85,\, 2.85]\times[-4.1,\, -3.9]$ (in km) and $\overline{\Omega_{\mathrm{fr}}}$ consisting of 5 rectangular fractures, as depicted in Figure A.1. All material properties (except for the fracture size and orientation) and initial and boundary conditions were the same as those for reservoir $\mathcal{R}^{\square}$, see Section 5 and Tables 1 and 2.

A.1.2 Artificial optimization setup

We performed an artificial optimization with $t_{\mathrm{ini}} = 0$ and $t_{\mathrm{fin}} = 60 \cdot 60 \cdot 24 \cdot 365 \cdot 50\,\mathrm{s} \approx 50\,\mathrm{years}$ and 4 well configurations indicated in Figure A.1. That is, the optimization consisted of only 4 optimization steps defined

configuration nr.	Δp	$\mathcal{P}$	t_{break}	$\mathcal{C}$	$\mathcal{C}_{\text{ana}}$
1.	63.63	5.083	-	$1.41 \cdot 10^{18}$	$1.33 \cdot 10^{18}$
2.	59.96	5.261	-	$1.06 \cdot 10^{18}$	$1.00 \cdot 10^{18}$
3.	55.58	5.454	35	$0.70 \cdot 10^{18}$	$0.67 \cdot 10^{18}$
4.	51.33	5.304	14	$0.35 \cdot 10^{18}$	$0.33 \cdot 10^{18}$

Table A.1: Quantities describing the artificial optimization results. They are (in this order) the configuration number, $\Delta p = \sum_{w \in \mathcal{W}_{\text{inj}} \cup \mathcal{W}_{\text{pro}}} \left| \Delta p|_w(t) \right|$ [MPa], resulting power $\mathcal{P}$ [MW], time of thermal breakthrough occurrence t_{break} [year], and cost of the best path between the wells denoted by $\mathcal{C}$ [1/m], and the theoretical minimum of $\mathcal{C}$ over all spatial meshes labeled $\mathcal{C}_{\text{ana}}$ [1/m], which can be computed analytically. In the first two configurations, the thermal breakthrough did not occur.

below.

All wells were $100\,\text{m}$ long and parallel to the z-axis. Their flow rates were $Q = \pm 30\, l/s$. The production well was fixed, and its barycenter coincided with the barycenter of 5. fracture, which is (in km) the point (0.0, 0.0, -4.0). The injection well in the i-th configuration ($i \in \{1, 2, 3, 4\}$) intersected the i-th fracture. The coordinates of the well barycenters (in km) were, in this order, (0.7, 0.0, -4.0), (0.0, 0.7, -4.0), (-0.7, 0.0, -4.0), and (0.0, -0.7, -4.0). The rest of the well properties equaled those listed in Table 2.

A.1.3 Parameters of numerical solver

The balance equations were solved with the time step $\Delta t = (t_{\text{fin}} - t_{\text{ini}})/50\,\text{s} \approx 1\,\text{year}$. The domain Ω_{fr} was covered with a boundary conforming Delaunay mesh of 15225 triangles with edge lengths in [6.2, 19.5] (in m). The domain Ω_{la} was covered with a boundary and fracture conforming Delaunay mesh of 4045788 tetrahedra with edge lengths in [6.2, 103.3] (in m), where each triangle was a face of two tetrahedra. Parts of these meshes are shown in Figure A.1. All wells had the artificial radius $r_\varepsilon = 7\,\text{m}$.

A.1.4 Results

The results are summarized in Table A.1. We can see that Δp decreased when narrowing the gap between the fractures intersecting the wells. The resulting power $\mathcal{P}$ would probably have monotonically increased with decreasing Δp if the narrowest gap between the fractures intersected by the wells had not caused a very early thermal breakthrough.

Additionally, when narrowing the above gap between the fractures, the cost of the best path, $\mathcal{C}$, decreases, fulfilling the requirements. This cost also seems to approach its theoretical minimum in the process. The probable reason is that the tetrahedral mesh between the fractures is coarser than the triangular meshes. Therefore, a shorter path through the 3D mesh implies a smaller deviation from the theoretical minimum cost.

We consider the results of this verification and validation test satisfactory.

A.2 Shelves

Using this test, we checked whether our framework satisfies the natural requirement that the energy E_{pump} given by (14) decreases if the area of the clusters of interconnected fractures crossed by the wells increases. Additionally, this test enabled us to check whether the reservoir characteristics are evaluated correctly.

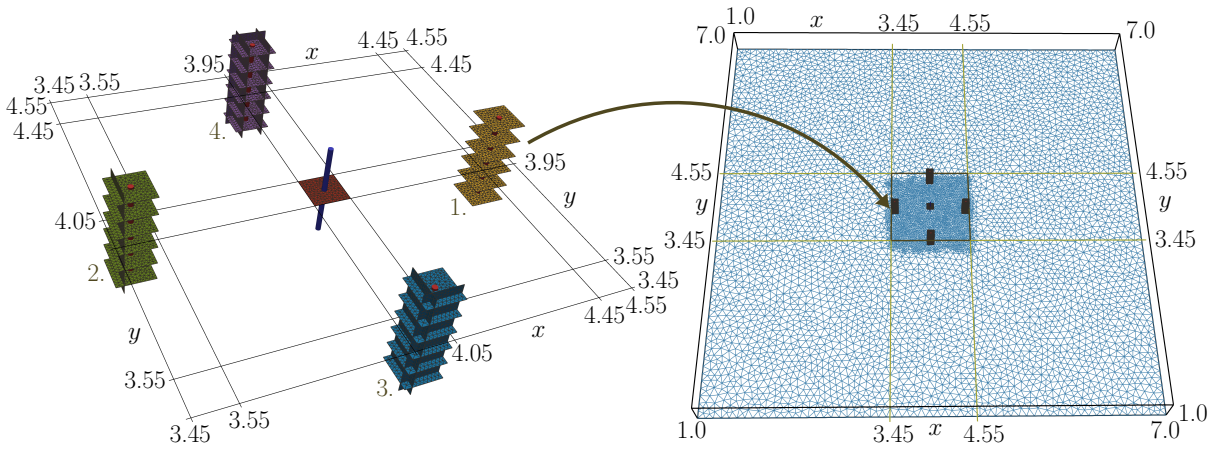

Figure A.2: **Left:** DFN consisting of 31 fractures, where 30 of them are aligned in columns labeled 1.–4., and wells in four different configurations indicated by numbers 1.–4. that coincide with the column labels. The triangulation of the DFN depicted in the figure was employed in the test. **Right:** Position of the DFN inside $\overline{\Omega_{\mathrm{la}}}$ indicated by the black prism. The blue lines stand for the triangulation of the bottom face of $\overline{\Omega_{\mathrm{la}}}$. All spatial coordinates are in km.

A.2.1 Reservoir setup

We considered $\overline{\Omega_{\mathrm{la}}} = [-1.0,\, 7.0] \times [-1.0,\, 7.0] \times [-4.2,\, -3.8]$ (in km) and $\overline{\Omega_{\mathrm{fr}}}$ consisting of 25 horizontal square fractures with a side length of 100 m and 6 vertical rectangular fractures with side lengths of 100 m and 300 m. All of the fractures were aligned with the coordinate axes. The situation is depicted in Figure A.2.

In what follows, all spatial coordinates are in km. The first horizontal fracture had its barycenter at (4.0, 4.0, -4.0), the barycenter of $\overline{\Omega_{\mathrm{la}}}$. The remaining 24 fractures were aligned in 4 vertical columns (labeled 1.–4.) of 6 fractures. The barycenters of the fractures in these columns were, in this order, (4.5, 4.0, -4.125 + $0.05i$), (3.5, 4.0, -4.125 + $0.05i$), (4.0, 3.5, -4.125 + $0.05i$), and (4.0, 4.5, -4.125 + $0.05i$), where $i = 0,\, 1,\, \ldots,\, 5$.

The i-th column of fractures was intersected by $i - 1$ of the above vertical fractures. These vertical fractures had the barycenters at (3.47, 4.0, -4.0) (2. column), (4.0, 3.47, -4.0) and (3.97, 3.5, -4.0) (3. column), and (4.0, 4.53, -4.0), (3.97, 4.5, -4.0), and (4.03, 4.5, -4.0) (4. column).

All material properties (except for the fracture size and orientation) were the same as those for reservoir $\mathcal{R}^{\square}$, see Section 5 and Tables 1 and 2.

The initial conditions were

$$p_{\mathrm{ini}}(x, y, z) = 101325.0\,\mathrm{Pa}, \quad T_{\mathrm{ini}}(x, y, z) = 404.66\,\mathrm{K}. \tag{A.1}$$

We employed these initial conditions to make the results less dependent on the vertical positions of the fractures inside the domain.

As for the boundary conditions, we prescribed the homogeneous Neumann boundary conditions on $\partial\Omega_{\mathrm{fr}}$ and on the faces of $\partial\Omega_{\mathrm{la}} \setminus \overline{\Omega_{\mathrm{fr}}}$ that lie in the planes $z = -4.2$ and $z = -3.8$ (in km). In the remainder of $\partial\Omega_{\mathrm{la}} \setminus \overline{\Omega_{\mathrm{fr}}}$, we considered the Dirichlet boundary conditions identical to the initial conditions.

A.2.2 Artificial optimization setup

We performed an artificial optimization with $t_{\mathrm{ini}} = 0$ and $t_{\mathrm{fin}} = 60 \cdot 60 \cdot 24 \cdot 365 \cdot 50\,\mathrm{s} \approx 50$ years and 4 well configurations indicated in Figure A.2. That is, the optimization consisted of only 4 optimization steps defined below.

column nr.	Δp	$\mathcal{P}$	$\lvert\#\rvert$	$\rho_{\times,\#}$	$l_\#$	$d_\#$
1.	121.85	4.875	$1.0 \cdot 10^4$	0.0	147.62	141.42
2.	121.08	4.951	$9.0 \cdot 10^4$	$6.67 \cdot 10^{-5}$	439.99	316.23
3.	120.47	5.012	$12.0 \cdot 10^4$	$10.83 \cdot 10^{-5}$	381.52	320.62
4.	120.10	5.048	$15.0 \cdot 10^4$	$13.33 \cdot 10^{-5}$	367.27	321.87

Table A.2: Quantities describing the artificial optimization results and characteristics of the column of fractures intersected by the production well. They are (in this order) the column/configuration number, $\Delta p = \sum_{w \in \mathcal{W}_{\text{inj}} \cup \mathcal{W}_{\text{pro}}} \left| \Delta p|_w(t) \right|$ [MPa], resulting power $\mathcal{P}$ [MW], area of the largest cluster of interconnected fractures within the column $\lvert\#\rvert$ [m^2], number of fracture intersections per total area of fractures within the column $\rho_{\times,\#}$ [1/m^2], and length $l_\#$ [m] and size $d_\#$ [m] of the largest cluster of interconnected fractures within the column.

All wells were 260 m long and parallel to the z-axis. Their flow rates were $Q = \pm 60\, l/s$. The production well was fixed, and its barycenter coincided with the barycenter of $\overline{\Omega_{\text{la}}}$, which is (in km) the point (4.0, 4.0, -4.0). The injection well in the i-th configuration ($i \in \{1, 2, 3, 4\}$) intersected the i-th column of fractures. The coordinates of the well barycenters (in km) were, in this order, (4.5, 4.0, -4.0), (3.5, 4.0, -4.0), (4.0, 3.5, -4.0), and (4.0, 4.5, -4.0). Hence, the wells intersected all horizontal fractures in the given column. The rest of the well properties equaled those listed in Table 2.

A.2.3 Parameters of numerical solver

The balance equations were solved with the time step $\Delta t = (t_{\text{fin}} - t_{\text{ini}})/50\,\text{s} \approx 1$ year. The domain Ω_{fr} was covered with a boundary conforming Delaunay mesh of 10744 triangles with edge lengths in [5.0, 20.0] (in m). The domain Ω_{la} was covered with a boundary and fracture conforming Delaunay mesh of 213332 tetrahedra with edge lengths in [5.0, 413.5] (in m), where each triangle was a face of two tetrahedra. Parts of these meshes are shown in Figure A.2. All wells had the artificial radius $r_\varepsilon = 7$ m.

A.2.4 Results

The results are summarized in Table A.2. We can see that Δp decreased when increasing the area of fractures within the column intersected by the production well, and the power $\mathcal{P}$ increased accordingly because, unlike in the test in Section A.1, the thermal breakthrough did not occur in any configuration.

Comparing the values of $l_\#$ and $d_\#$ for columns 2–4, we can see that when adding the vertical fractures to the cluster of the interconnected fractures, $d_\#$ increased because the cluster extended, but $l_\#$ decreased because the fractures became better connected. In the case of column 1, the difference between $d_\#$ (the length of a square diagonal) and $l_\#$ illustrates the dependence of $l_\#$ on the spatial mesh. The theoretical minimum of $l_\#$ equals $d_\#$ in this case.

We consider the results of this verification and validation test satisfactory.

References

[1] Pasquale C. Africa, Daniel Arndt, Wolfgang Bangerth, Bruno Blais, Marc Fehling, Rene Gassmöller, Timo Heister, Luca Heltai, Sebastian Kinnewig, Martin Kronbichler, Matthias Maier, Peter Munch, Magdalena Schreter-Fleischhacker, Jan P. Thiele, Bruno Turcksin, David Wells, and Vladimir Yushutin. The deal.II library, version 9.6. *Journal of Numerical Mathematics*, 32(4):369–380, 2024.

[2] Thorsten Agemar, Rüdiger Schellschmidt, and Rüdiger Schulz. Subsurface temperature distribution in Germany. *Geothermics*, 44:65–77, 2012.

[3] Thorsten Agemar, Josef Weber, and Rüdiger Schulz. Deep geothermal energy production in Germany. *Energies*, 7(7):4397–4416, 2014.

[4] James Ahrens, Berk Geveci, and Charles Law. ParaView: An end-user tool for large data visualization. *Visualization Handbook*, 2005.

[5] Masoud Babaei and Hamidreza M. Nick. Performance of low-enthalpy geothermal systems: Interplay of spatially correlated heterogeneity and well-doublet spacings. *Applied Energy*, 253:113569, 2019.

[6] Gabriel R. Barrenechea, Volker John, and Petr Knobloch. Finite element methods respecting the discrete maximum principle for convection-diffusion equations. *SIAM Review*, 66(1):3–88, 2024.

[7] Inga Berre, Florian Doster, and Eirik Keilegavlen. Flow in fractured porous media: A review of conceptual models and discretization approaches. *Transport in Porous Media*, 130:215–236, 2019.

[8] Laura Blank, Ernesto Meneses Rioseco, Alfonso Caiazzo, and Ulrich Wilbrandt. Modeling, simulation, and optimization of geothermal energy production from hot sedimentary aquifers. *Computational Geosciences*, 25:67–104, 2021.

[9] J. Bundschuh and M.C. Suárez Arriaga. *Introduction to the numerical modeling of groundwater and geothermal systems - Fundamentals of mass, energy and solute trasport in poroelastic rocks*. CRC Press. Taylor & Francis Group, Boca Raton, Florida, USA, 2010.

[10] Meng Cao, Sho Hirose, and Mukul M. Sharma. Factors controlling the formation of complex fracture networks in naturally fractured geothermal reservoirs. *Journal of Petroleum Science and Engineering*, 208:109642, 2022.

[11] Hank Childs, Eric Brugger, Brad Whitlock, Jeremy Meredith, Sean Ahern, David Pugmire, Kathleen Biagas, Mark C. Miller, Cyrus Harrison, Gunther H. Weber, Hari Krishnan, Thomas Fogal, Allen Sanderson, Christoph Garth, E. Wes Bethel, David Camp, Oliver Rubel, Marc Durant, Jean M. Favre, and Paul Navratil. VisIt: An end-user tool for visualizing and analyzing very large data. `https://visit.llnl.gov`, 2012.

[12] H.-J. G. Diersch. *Finite Element Modeling of Flow, Mass and Heat Transport in Porous and Fractured Media*. Springer Berlin, Heidelberg, 2014.

[13] M. Dussel, E. Lüschen, R. Thomas, T. Agemar, T. Fritzer, S. Sieblitz, B. Huber, J. Birner, and R. Schulz. Forecast for thermal water use from Upper Jurassic carbonates in the Munich region (South German Molasse Basin). *Geothermics*, 60:13–30, 2016.

[14] Mohamed Fadel, Ernesto Meneses Rioseco, Pierre-Olivier Bruna, and Inga Moeck. Pressure transient analysis to investigate a coupled fracture corridor and a fault damage zone causing an early thermal breakthrough in the North Alpine Foreland Basin. *Geoenergy Science and Engineering*, 229:212072, 2023.

[15] Alessandro Franco and Maurizio Vaccaro. Numerical simulation of geothermal reservoirs for the sustainable design of energy plants: A review. *Renewable and Sustainable Energy Reviews*, 30:987–1002, 2014.

[16] M. Frey, K. Bär, I. Stober, J. Reinecker, J. van der Vaart, and I. Sass. Assessment of deep geothermal research and development in the Upper Rhine Graben. *Geothermal Energy*, 10(18), 2022.

[17] Alessio Fumagalli, Eirik Keilegavlen, and Stefano Scialò. Conforming, non-conforming and non-matching discretization couplings in discrete fracture network simulations. *Journal of Computational Physics*, 376:694–712, 2019.

[18] Christophe Geuzaine and Jean-François Remacle. Gmsh: A 3-D finite element mesh generator with built-in pre- and post-processing facilities. *International Journal for Numerical Methods in Engineering*, 79(11):1309–1331, 2009.

[19] Dennis Gläser, Bernd Flemisch, Holger Class, and Rainer Helmig. Frackit: a framework for stochastic fracture network generation and analysis. *Journal of Open Source Software*, 5:2291, 2020.

[20] S. Homuth, A. E. Götz, and I. Sass. Reservoir characterization of the Upper Jurassic geothermal target formations (Molasse Basin, Germany): role of thermofacies as exploration tool. *Geothermal Energy Science*, 3:41–49, 2015.

[21] Jeffrey D. Hyman, Satish Karra, Nataliia Makedonska, Carl W. Gable, Scott L. Painter, and Hari S. Viswanathan. dfnWorks: A discrete fracture network framework for modeling subsurface flow and transport. *Computers & Geosciences*, 84:10–19, 2015.

[22] International Renewable Energy Agency (IRENA). Global geothermal market and technology assessment, 2023.

[23] Abhinav Jha, Ondřej Pártl, Naveed Ahmed, and Dmitri Kuzmin. An assessment of solvers for algebraically stabilized discretizations of convection–diffusion–reaction equations. *Journal of Numerical Mathematics*, 31(2):79–103, 2023.

[24] L. Jin and M. D. Zoback. Fully coupled nonlinear fluid flow and poroelasticity in arbitrarily fractured porous media: A hybrid-dimensional computational model. *Journal of Geophysical Research: Solid Earth*, 122(10):7626–7658, 2017.

[25] Steven G. Johnson. The NLopt nonlinear-optimization package. `https://github.com/stevengj/nlopt`, 2007.

[26] M. Karimi-Fard, L. J. Durlofsky, and K. Aziz. An efficient discrete-fracture model applicable for general-purpose reservoir simulators. *SPE Journal*, 9(02):227–236, 06 2004.

[27] Eirik Keilegavlen, Runar Berge, Alessio Fumagalli, Ivar Stefansson, Julian Huber, and Inga Berre. PorePy: an open-source software for simulation of multiphysics processes in fractured porous media. *Computational Geosciences*, 25:243–265, 2021.

[28] Timo Koch, Dennis Gläser, Kilian Weishaupt, Sina Ackermann, Martin Beck, Beatrix Becker, Samuel Burbulla, Holger Class, Edward Coltman, Simon Emmert, Thomas Fetzer, Christoph Grüninger, Katharina Heck, Johannes Hommel, Theresa Kurz, Melanie Lipp, Farid Mohammadi, Samuel Scherrer, Martin Schneider, Gabriele Seitz, Leopold Stadler, Martin Utz, Felix Weinhardt, and Bernd Flemisch. DuMux 3 – an open-source simulator for solving flow and transport problems in porous media with a focus on model coupling. *Computers & Mathematics with Applications*, 81:423–443, 2021.

[29] Olaf Kolditz, Sebastian Bauer, Lars Bilke, Niels Böttcher, Jens-Olaf Delfs, Tobias Fischer, Uwe Janos Görke, Thomas Kalbacher, Georg Kosakowski, Christopher McDermott, C. H. Park, F. Radu, Karsten Rink, He Shao, Fuxiang Sun, Yingqi Sun, A. K. Singh, J. Taron, M. Walter, Wenqing Wang, Norihiro Watanabe, Yu-Shu Wu, Mingjie Xie, W. Xu, and Björn Zehner. OpenGeoSys: an open-source initiative for numerical simulation of thermo-hydro-mechanical/chemical (THM/C) processes in porous media. *Environmental Earth Sciences*, 67:589–599, 2012.

[30] F. Konrad, A. Savvatis, F. Wellmann, and K. Zosseder. Hydraulic behavior of fault zones in pump tests of geothermal wells: a parametric analysis using numerical simulations for the Upper Jurassic aquifer of the North Alpine Foreland Basin. *Geothermal Energy*, 7:25, 2019.

[31] Florian Konrad, Alexandros Savvatis, Denise Degen, Florian Wellmann, Florian Einsiedl, and Kai Zosseder. Productivity enhancement of geothermal wells through fault zones: Efficient numerical evaluation of a parameter space for the Upper Jurassic aquifer of the North Alpine Foreland Basin. *Geothermics*, 95:102119, 2021.

[32] Hans-Joachim Kretzschmar and Wolfgang Wagner. *International Steam Tables: Properties of water and steam based on the industrial formulation IAPWS-IF97*. Springer Berlin, Heidelberg, 2014.

[33] J.F. Krumbholz, M. Krumbholz, S.H. Wadas, and D.C. Tanner. Characterisation of the fracture- and karst-controlled geothermal reservoir below Munich from geophysical wireline and well information. *Geothermal Energy*, 12:9, 2024.

[34] P. S. Lang, A. Paluszny, and R. W. Zimmerman. Permeability tensor of three-dimensional fractured porous rock and a comparison to trace map predictions. *Journal of Geophysical Research: Solid Earth*, 119(8):6288–6307, 2014.

[35] J.C. Lorenz and S.P. Cooper. *Applied Concepts in Fractured Reservoirs*. John Wiley & Sons Ltd, 2020.

[36] Saeed Mahmoodpour, Mrityunjay Singh, Kristian Bär, and Ingo Sass. Impact of well placement in the fractured geothermal reservoirs based on available discrete fractured system. *Geosciences*, 12(1), 2022.

[37] Xenia Malcher and Miguel Gonzalez-Salazar. Strategies for decarbonizing European district heating: Evaluation of their effectiveness in Sweden, France, Germany, and Poland. *Energy*, 306:132457, 2024.

[38] N. Mantei, E. Meneses Rioseco, and I. S. Moeck. Parametric analysis of geothermal reservoir performance in Mesozoic sandstone formations within the North German Basin developed by multi-well systems. *Geothermal Energy*, 13(26):26, 2025.

[39] Ernesto Meneses Rioseco, Michael Dussel, and Inga S. Moeck. 3D thermo-hydro-mechanical simulation of the behaviour of a naturally fractured petrothermal reservoir in deep Upper Jurassic carbonates of the Bavarian Molasse Basin – Case study Geretsried. *Geomechanics and Tunnelling*, 15(1):48–57, 2022.

[40] Inga S. Moeck. Catalog of geothermal play types based on geologic controls. *Renewable and Sustainable Energy Reviews*, 37:867–882, 2014.

[41] Ali Moinfar, Abdoljalil Varavei, Kamy Sepehrnoori, and Russell T. Johns. Development of an efficient embedded discrete fracture model for 3D compositional reservoir simulation in fractured reservoirs. *SPE Journal*, 19(02):289–303, 07 2013.

[42] Wayne Narr, David S. Schechter, and Laird B. Thompson. *Naturally Fractured Reservoir Characterization*. Society of Petroleum Engineers, 2006.

[43] Ronald A. Nelson. *Geological Analysis of Naturally Fractured Reservoirs*. Gulf Professional Publishing, 2nd edition, 2001.

[44] Donald A. Nield and Adrian Bejan. *Convection in Porous Media*. Springer, New York, 3rd edition, 2006.

[45] B. Norden, A. Förster, H. J. Förster, and Sven Fuchs. Temperature and pressure corrections applied to rock thermal conductivity: impact on subsurface temperature prognosis and heat-flow determination in geothermal exploration. *Geothermal Energy*, 8:1(1), 2020.

[46] Ondřej Pártl and Ernesto Meneses Rioseco. Geothermal well placement optimization for sustainable energy production: New computational framework for fracture-controlled reservoirs. In *proceedings of EGU 2025 xxx*, page xx, EGU.

[47] Ondřej Pártl and Ernesto Meneses Rioseco. Efficient numerical framework for geothermal energy production optimization in fracture-controlled reservoirs. *International Journal for Numerical Methods in Fluids*, xx(x):xx, IJNMF.

[48] Charles S. Peskin. The immersed boundary method. *Acta Numerica*, 11:479–517, 2002.

[49] Robert Pitz-Paal, Joachim Krüger, Juliane Hinsch, Ahmet Lokurlu, Martin Scheuerer, Martin Schlecht, Mark Schmitz, and Gustl Schreiber. Decarbonizing the German industrial thermal energy use with solar, hydrogen, and other options–recommendations for the world. *Solar Compass*, 3-4:100029, 2022.

[50] Valentina Romano, Sabina Bigi, Francesco Carnevale, Jeffrey De'Haven Hyman, Satish Karra, Albert J. Valocchi, Maria Chiara Tartarello, and Maurizio Battaglia. Hydraulic characterization of a fault zone from fracture distribution. *Journal of Structural Geology*, 135:104036, 2020.

[51] T.H. Sandve, I. Berre, and J.M. Nordbotten. An efficient multi-point flux approximation method for discrete fracture–matrix simulations. *Journal of Computational Physics*, 231(9):3784–3800, 2012.

[52] Kamy Sepehrnoori, Yifei Xu, and Wei Yu. *Embedded Discrete Fracture Modeling and Application in Reservoir Simulation*, volume 68 of *Developments in Petroleum Science*. Elsevier, Amsterdam, 2020.

[53] Hang Si. TetGen, a Delaunay-based quality tetrahedral mesh generator. *ACM Transactions on Mathematical Software*, 41(2), feb 2015.

[54] Silvia De Simone, Caroline Darcel, Hossein A. Kasani, Diego Mas Ivars, and Philippe Davy. Equivalent Biot and Skempton poroelastic coefficients for a fractured rock mass from a DFN approach. *Rock Mechanics and Rock Engineering*, 56:8907–8925, 2023.

[55] John C. Slattery. *Advanced Transport Phenomena*. Cambridge University Press, 1st edition, 1999.

[56] Geertje Strijker, Giovanni Bertotti, and Stefan M. Luthi. Multi-scale fracture network analysis from an outcrop analogue: A case study from the Cambro-Ordovician clastic succession in Petra, Jordan. *Marine and Petroleum Geology*, 38(1):104–116, 2012.

[57] C. A. Vargas, L. Caracciolo, and P. J. Ball. Geothermal energy as a means to decarbonize the energy mix of megacities. *Communications Earth & Environment*, 3:66, 2022.

[58] Jeanne Vidal and Albert Genter. Overview of naturally permeable fractured reservoirs in the central and southern Upper Rhine Graben: Insights from geothermal wells. *Geothermics*, 74:57–73, 2018.

[59] Hongwei Wang, Hejuan Liu, Dongfang Chen, Haidong Wu, and Xianpeng Jin. Thermal response of the fractured hot dry rocks with thermal-hydro-mechanical coupling effects. *Geothermics*, 104:102464, 2022.

[60] Yao Wenli, Mostafa Sharifzadeh, Zhen Yang, Guang Xu, and Zhigang Fang. Assessment of fracture characteristics controlling fluid flow performance in discrete fracture networks (DFN). *Journal of Petroleum Science and Engineering*, 178:1104–1111, 2019.

[61] U. Wilbrandt, C. Bartsch, N. Ahmed, N. Alia, F. Anker, L. Blank, A. Caiazzo, S. Ganesan, S. Giere, G. Matthies, R. Meesala, A. Shamim, J. Venkatesan, and V. John. Parmoon – a modernized program package based on mapped finite elements. *Computers and Mathematics with Applications*, 74:74–88, 2016.

[62] Markus Wolfgramm, Matthias Franz, and Thorsten Agemar. Explorationsstrategie tiefer geothermischer Ressourcen am Beispiel des norddeutschen Beckens. In Mathias Bauer, Willi Freeden, Hans Jacobi, and Thomas Neu, editors, *Handbuch Tiefe Geothermie: Prospektion, Exploration, Realisierung, Nutzung*, pages 463–505. Springer Berlin Heidelberg, Berlin, Heidelberg, 2014.

[63] Chi Yao, Yulong Shao, Jianhua Yang, Fan Huang, Chen He, Qinghui Jiang, and Chuangbing Zhou. Effects of fracture density, roughness, and percolation of fracture network on heat-flow coupling in hot rock masses with embedded three-dimensional fracture network. *Geothermics*, 87:101846, 2020.

[64] Joël M. Zinsalo, Louis Lamarche, and Jasmin Raymond. Injection strategies in an enhanced geothermal system based on discrete fractures model. *Applied Thermal Engineering*, 169:114812, 2020.